Regional Responses to Oceanic Variability Constrain Global Drought Synchrony

Udit Bhatia[1,4] Hemant Poonia[1], Danish Mansoor Tantary[1], Vimal Mishra[1,2], Rohini Kumar[3],*
[1]Department of Civil Engineering, Indian Institute of Technology Gandhinagar, India
[2]Department of Earth Sciences, Indian Institute of Technology Gandhinagar, India
[3]Department of Computational Hydrosystems (CHS), Helmholtz Centre for Environmental Research - UFZ, Permoserstr.15, 04318 Leipzig, Germany
[4]Department of Computer Science and Engineering, Indian Institute of Technology Gandhinagar, India

Abstract

Synchronized droughts threaten global food security, with concerns about increased frequency and duration under climate change. However, their long-term evolution and physical limits remain unknown. We analyze 61 drought networks over 120 years (1901–2020) of sc-PDSI data, employing a suite of network synchronization measures and empirical orthogonal functions to unravel the physical drivers and limiters of drought synchrony. Our results show that, contrary to claims that synchronized droughts could affect up to one sixth of the global land mass, the maximum synchronized area fluctuates between 1. 84% and 6. 5% of the total land mass. Although we observe a strong dependence between drought onset and local crop failures, global drought synchrony is shaped by a dichotomy: temperature trends exacerbate it, while precipitation variability, modulated by sea surface temperature oscillations, limits it. This suggests that although drought hubs are increasing, large-scale synchronization across multiple agricultural regions is less widespread than expected, affecting global food security strategies.

Teaser

Temperature exacerbates drought synchrony, while rainfall variability mediates and limits its global extent.

Introduction

Droughts have severe impacts on water resources, agriculture, energy production, and various socioeconomic activities, making them among the most devastating natural disasters [1, 2]. Unlike many other natural hazards, droughts are slow-onset events, but their impacts can escalate rapidly and catastrophically when they persist [3, 4]. The synchronous occurrence of droughts across multiple regions, particularly in global breadbaskets, poses a significant threat to food security and economic stability on a global scale [5, 6]. As global temperatures are expected to rise, the frequency of droughts and associated risks of staple crop failure are also projected to increase [6, 7]. For example, conditional probabilities of crop failure for wheat, rice, maize, and soybeans under moderate drought conditions (sc-PDSI) range from 25–51

Addressing food security risks associated with synchronized droughts is critical for achieving Sustainable Development Goal (SDG) 2 (Zero Hunger) and SDG 13 (Climate Action). Although global temperatures are projected to increase, trends in precipitation and soil moisture exhibit significant regional variability, leading to diverse and region-specific drought impacts [5, 8–11]. This variability underscores the necessity to investigate the historical evolution of synchronized droughts and identify their regional and global drivers and constraints.

Recent advances in complex network analysis and causal discovery have significantly improved our understanding of synchronous extreme weather events [12]. These techniques have elucidated the synchronization patterns of extreme rainfall events and heatwaves globally [13–17]. Similarly, recent drought studies using complex networks have identified influential drought hubs in regions like southern Europe, northeast Brazil, Australia, and northwest USA [18]. However, most studies, such as Chauhan et al. (2024)[19], rely primarily on indices like the Standardized Precipitation Index (SPI), which consider only precipitation, neglecting critical factors such as temperature, evaporation, and soil moisture essential for comprehensive drought assessment[1].

Furthermore, previous analyses often focus on single or limited time periods, leaving the temporal evolution of synchronized droughts largely unexplored. Linear methods, including Empirical Orthogonal Functions (EOFs) and Maximum Covariance Analysis (MCA), have effectively identified climate variability patterns linked to large-scale oscillations like El Niño-Southern Oscillation (ENSO) [20–23]. Nevertheless, relying solely on linear methods might overlook complex and evolving regional drought connections.

Prior research has also noted uncertainties in drought trend detection due to variations in drought indices and methodological choices. For example, Sheffield et al.[24] questioned the robustness of traditional PDSI formulations, reporting minimal global drought changes over recent decades. Conversely, Dai[25] found increasing global drought trends associated explicitly with global warming. Such differences highlight the sensitivity of drought assessments to the choice of methods and indices, underscoring the need for analyses that complement these approaches.

To address these critical gaps, our study adopts a complementary yet distinct perspective by analyzing the synchronized evolution of drought conditions across regions. We employ both linear and non-linear methods, including Maximum Covariance Analysis (MCA) and event synchronization-based complex network analysis, to comprehensively explore the spatio-temporal dynamics of meteorological droughts and their climatic drivers from 1901 to 2020. Specifically, our study addresses three key research questions: (a) How have globally synchronous drought patterns evolved over the past century in response to large-scale climatic variability? (b) How does regional connectivity contribute to global drought synchronization? and (c) How do temperature and precipitation interactions shape synchronous global drought development?

Using the self-calibrated Palmer Drought Severity Index (sc-PDSI), which integrates multiple climate variables and provides a more comprehensive representation of drought conditions, our analysis reveals how global drought connectivity has evolved under changing climatic conditions. Our findings highlight increased connectivity among drought-prone regions, suggesting higher risks of synchronous droughts in a warming world, moderated by regional rainfall variability driven by sea surface temperature (SST) patterns. Ultimately, our study advances the understanding of drought synchrony by providing insights into the large-scale propagation and intensification mechanisms of drought, supporting targeted resilience strategies for global food security and climate adaptation.

Results

Global Patterns of Crop Yield Failures Under Moderate Drought Conditions

We conducted a conditional probability analysis between crop yield anomalies and moderate drought conditions (sc-PDSI ≤ -2) using a global dataset that integrates observed and satellite-based historical yield data (V1.2 and V1.3) [26] at a 0.5-degree resolution for four staple crops: wheat, rice, maize, and soybeans. The analysis was carried out at each grid point where food production data is available. For the 36-year period, We calculated the number of events where both crop yield fell below the long-term mean minus 0.5 times the standard deviation, and the average sc-PDSI during the growing season was less than -2. Our results reveal that conditional probabilities of crop failure exceed 50% at several key food-producing regions (Figure 1). For maize, high probabilities($\geq$ 35%) are observed across multiple continents, including regions such as the United States Corn Belt, Southern China, and parts of Southeast Asia (Fig. 1C). Similarly, soybean shows failure probabilities over 40% in South America, particularly Brazil and Argentina, as well as in parts of the North America (Fig. 1D). Wheat exhibits failure probabilities ranging from 27 to 40% (Supplementary Table 1) in regions such as the northern plains of the United States, Canada, Eastern Europe, and Central Asia (Fig. 1A). Rice, predominantly grown in South Asia, Southeast

Asia, and sub-Saharan Africa, faces failure probabilities ranging from 25 to 36%, with monsoonal rainfall disruptions posing significant risks to production, particularly in countries like India and Indonesia (Fig. 1B). Similar insights were obtained from the analysis of crop yields falling below a threshold (mean - 1 standard deviation) and sc-PDSI averaged over entire nations using copula methods (see Methods and SI Fig. 1).

Global patterns demonstrate the significant impact of droughts on agricultural production, with at least one major crop in each of the world's key food-producing regions in the world shown to be at a risk of failure during moderate droughts. While these results highlight the connection between drought conditions and crop failures at both local and national scales, they do not offer conclusive insights into whether these regions are likely to experience synchronized droughts on a global scale. Although the joint dependence between sc-PDSI and crop failure is evident, the broader question of whether drought events (and their impact) could align globally, potentially threatening food security, remains unresolved, which is discussed next.

Temporal Evolution of Drought Networks

To understand the evolution and structure of global synchronous droughts, we analyzed the spatio-temporal connectivity of drought events over the full period from 1901 to 2020 using complex network analysis. We constructed a network of moderate drought-onset events (sc-PDSI $\leq$ -2) using the event synchronization technique described in [27]. Fig. 2A shows the degree centrality of each node, corrected for projection distortions (original values provided in Supplementary Fig. S2). The network reveals a heterogeneous connectivity structure, with prominent drought hubs in regions such as South Africa, western North America, Australia, the Middle East, and South America, consistent with key climatic features such as the Botswana High, Bolivian High, Bilybara High, and North Pacific High [18, 28]. Singh et al.(2022) [29] have shown that increased ENSO variability in a warming climate heightens the risk of concurrent regional droughts. However, the implications of this variability on the synchronization of droughts on a global scale remain unclear.

To examine the impact of oceanic variability on drought synchronization, we segregated El Niño and La Niña years using historical ENSO classifications based on the Extended Multivariate ENSO Index (Supplementary Table 2) and constructed two separate synchronization networks. The analysis shows that South America and Australia consistently act as drought hubs, but the prominence of these hubs fluctuates significantly between El Niño and La Niña years (Fig. 3(A) and 3(B),Table 1). During El Niño, Australia exhibits a much higher drought degree (732) compared to La Niña (127), reflecting its heightened sensitivity to El Niño-induced moisture deficits and the weakening of the Walker circulation. Conversely, Africa and South America display increased drought degree during La Niña years, with South America showing a marked rise from 201 in El Niño to 301 in La Niña years. This shift in the geographic distribution of droughts during La Niña supports the observation that La Niña tends to drive more dispersed and fragmented drought patterns, whereas El Niño induces more concentrated but intense droughts. Furthermore, the spatial extent of drought onset, measured through the average link length (ALL) between drought events (Fig. 3(C) and 3(D),Table 1), is generally greater during La Niña years, particularly in Africa and Asia. This suggests that La Niña disperses the geographic impacts of drought, altering drought synchrony. In contrast, regions like Europe and North America exhibit relatively stable drought patterns, with only moderate changes in ALL during La Niña. These results indicate that oceanic variability, particularly ENSO phases, introduces asynchronous regional responses, ultimately limiting the global extent of drought synchronization.

To understand regional connectivity within the network, we evaluated the local clustering coefficient, an indicator of how connected neighbors are to each other, providing insight into the degree of local interconnectedness (Supplementary Fig. S3(A)). Regions with high clustering coefficients, such as Australia and Southern Africa, show strong internal connections, indicating local-scale synchronization [30]. In contrast, South America exhibits high degree centrality but low clustering, indicating sparse local networks with greater reliance on large-scale teleconnections. We also quantified the spatial extent of drought synchronization using the average link length (ALL) (Supplementary Fig. S3(B)), which measures the mean distance between the connected nodes. ALL values range from several hundred to 20,000 kilometers, indicating connections from regional to global scales. Coastal regions like western North America and eastern South America exhibit higher ALL, suggesting stronger teleconnections influenced by oceanic and atmospheric processes. In contrast, the interior regions of South America, constrained by topographic barriers such as the Andes, show lower ALL, indicating more localized synchronization.

To assess changes in network structure over time, we employed the methodology outlined in [16], constructing 61 network instances using a 60-year sliding window starting from 1901. Fig. 2B shows the degree centrality distribution across different periods, revealing a heavy-tailed distribution indicative of hubs. As the frequency of drought increases (Supplementary Fig. S4), the distribution shifts to the right (Supplementary Table 3), with high degree nodes becoming more common, indicating increased connectivity among drought-affected regions and a reduction in zero-degree nodes (Supplementary Fig. S5), signifying more nodes (or drought-affected areas) actively participating in the network over time. For example, the mean degree centrality increased from 96 during the 1901–1960 period to 147 during 1961–2020, reflecting a significant increase in network connectivity. Fig. 2C shows that a Mann-Kendall trend test indicates 54% of the nodes exhibit increasing degree trends, while 23.5% show decreasing trends. Furthermore, the probability of observing a degree centrality greater than the 90th quantile ($\Pr(\text{Deg} \geq 357)$) increased 1.36 times, increasing from 0.0347 in 1901–1960 to 0.0474 in 1961–2020. This shift underscores the growing inter connectivity of drought-affected regions, with more than half of the regions becoming increasingly interconnected, potentially leading to more widespread and synchronized drought events.

Further analysis of regional variations in degree trends on the continental scale (Supplementary Table 4) reveals that Australia exhibits the most significant increase in positive degree trends (88% of nodes), compared to 52% in South America. Fig. 2D presents box plots of degree centrality across three periods, highlighting increases in mean degree, particularly in earlier periods. However, the more modest increase in degree during the second period (1961–2020) suggests that oceanic and regional variability may constrain global drought synchronization. The maximum degree centrality observed was 3871 (6.5% of the total grid cells) during the 1942–2001 period, in contrast to previous studies that reported degree centralities as high as 15,000 [18]. The extent to which oceanic variability permits such extensive connectivity remains a question we explore further.

SST Drivers of Drought Variability

Building on the network analysis of global synchronous droughts, we examine the role of sea surface temperature anomalies (SST) in shaping drought patterns using Maximum Covariance Analysis (MCA)[20, 31]. This approach identifies the dominant modes of variability that link SST anomalies with global sc-PDSI patterns. The first mode, shown in Fig. 3A), is strongly associated with the El Niño-Southern Oscillation (ENSO), which explains around 37.6% of squared covariance and their PCs are strongly correlated exhibiting a significant correlation (r = 0.85, $p < 0.05$) [32]. ENSO phases exert a well-established influence on global weather, with contrasting impacts across regions. For instance, during El Niño events, Peru and Ecuador experience increased rainfall, while northeastern South America faces drought conditions[33]. In India, ENSO weakens monsoon rainfall, and warming of the tropical Indian Ocean exacerbates this effect [20, 34]. Similarly, Australia experiences drought as El Niño disrupts convective rainfall. In Europe, variability driven by the North Atlantic Oscillation (NAO) and Tropical North Atlantic (TNA) modes leading to warmer and wetter conditions in the north, while the south Europe experiences cooler and drier conditions [35, 36].

The second mode, shown in Supplementary Fig. S6, also exhibits ENSO-driven characteristics and The Principal Components (PCs) of SST anomalies and sc-PDSI anomalies shows a correlation of 0.79 ($p < 0.05$) explaining 15.2% of the squared covariance. This mode emphasizes the region-specific nature of SST-drought linkages. For example, in Australia, cooler central Pacific SSTs and negative IOD phases reduce drought severity, while in the Indian subcontinent, SST pattern correlates with dipolar drought structure with with wet conditions over the Indo-Gangetic plains and drought like condition over the southern part of India. In Africa, contrasting responses are observed, with positive correlations in the southern regions of Africa and negative correlations in the Sahel, reflecting localized influences.

These modes highlight the spatial variability of SST influences, with the first mode showing positive correlations in North America, Europe, and South America, and negative correlations in Africa, Australia, and Asia (Fig. 3A). The second mode reveals distinct impacts in Australia and Asia (Supplementary Fig. S6). The contrasting correlations across regions indicate a duality that reflects broken synchrony in global drought patterns, where warming in one oceanic region can simultaneously drive drought in one area while mitigating it in another.

Changing Role of Large-Scale Climate Variability in Drought Patterns

As noted previously (Fig. 2), the latter half of the twentieth century shows a significant increase in drought synchrony, reflected in both degree centrality and link length. To further explore the relationship between sea surface temperature (SST) anomalies and sc-PDSI, we performed a singular value decomposition (SVD) analysis for two periods: 1901–1960 and 1961–2020. During the first period, strong correlations were observed between the SST departure field and sc-PDSI in the central Pacific and Indian Oceans (Fig. 4), consistent with an El Niño-Southern Oscillation (ENSO) pattern. This mode remains dominant in the second period (Fig. 4B), exhibiting an increased influence, as the Squared Covariance Factor (SCF) for this leading mode rose from 32% to 38.8%, highlighting the strengthening of the ENSO and sc-PDSI relationship. Comparing these two periods suggests distinct shifts in the correlation patterns within the Indian and Atlantic Oceans, indicating a growing impact of oceanic variability on global drought synchronization.

The second mode, shown in Supplementary Fig. S7, also exhibits increased influence, with the SCF rising from 16.1% to 17.6%. Changes are particularly evident in the Tropical North Atlantic, highlighting the evolving role of SST variability in shaping global drought patterns.

Temperature Exacerbates, Rainfall Variability Modulates Global Drought Synchronization

Given that sc-PDSI as a drought indicator is derived from precipitation and temperature anomalies, together with modulation by land surface properties [37], it is crucial to understand how these driving variables interact with sea surface temperature (SST) to influence global drought patterns. To investigate these interactions, we performed maximum covariance analysis (MCA) on the SST departure field with precipitation (P) and air temperature (T) from 1901 to 2020.

The first leading mode of variability between global precipitation and SST anomalies (Fig. 5A) exhibits varying signs on all continents, reflecting regional differences in response to SST variability. In contrast, the temperature-SST correlations (Fig. 5B) consistently display the same sign globally, underscoring the dominant influence of increasing global temperatures. The first mode for P-SST explains 65.6% of the squared covariance, with the principal components strongly correlated ($r = 0.92$, $p < 0.05$), and captures the characteristic pattern of the El Niño-Southern Oscillation (ENSO). SST anomalies in the equatorial Pacific show opposite signs compared to precipitation anomalies in regions such as Australia, Southeast Asia, and Africa. This pattern is consistent with previous findings [20, 33], underscoring the central role of ocean variability in modulating global precipitation patterns.

In the second mode (Supplementary Fig. S8), which accounts for 8.94% ($r = 0.85$) of the SCF for precipitation and 18.8% ($r = 0.67$) for temperature, the P-SST correlations continue to display contrasting signs across continents, underscoring the regional variability that influences drought patterns. In contrast, the T-SST correlations remain consistent between regions, further emphasizing the widespread impact of rising temperatures globally. These findings indicate that while SST variability drives the increasing spatial extent of synchronous droughts, regional differences in precipitation correlations serve as a key modulating factor, limiting the overall degree of synchronization.

Thus, while temperature exacerbates the consistency of drought patterns, precipitation variability modulates their spatial distribution, reducing overall synchrony. The evolving regional climate interactions underscore the importance of further investigating the processes behind these shifts, particularly as global temperatures continue to rise.

Relative Roles of Precipitation and Temperature in Driving Drought Trends

Drought synchrony can increase either due to precipitation deficits becoming more spatially coherent or through rising temperatures uniformly enhancing evaporative demand. To quantify the relative roles of these two mechanisms, we partitioned observed drought severity trends—quantified by the self-calibrating Palmer Drought Severity Index (scPDSI)—into precipitation-driven and temperature-driven components. For this analysis, we used monthly global precipitation and temperature data from the CRU TS v4.07 dataset spanning 1901–2021. Potential evapotranspiration (PET) was calculated using the Thornthwaite method (see Methods, "Trend-partition experiments"). We chose this method specifically because it relies solely on temperature, thus isolating the influence of temperature-driven evaporative demand from other meteorological variables such as wind speed, humidity, and radiation included in alternative PET methods. Linear trends in scPDSI were estimated using the non-parametric Sen's slope estimator (see Methods).

Globally, precipitation accounted for approximately two-thirds of the multi-decadal drought severity trends, with contributions remaining consistent at around 66% for 1961–1990 and 67% for 1991–2020 (Fig. 7E). Temperature-driven evaporative demand explained the remaining one-third. At regional scales, precipitation remained the predominant driver, notably in Australia and South America, consistently accounting for more than 75% of the observed trends across both periods (Fig. 7B,D). However, the contribution from temperature-driven evaporation notably increased post-1990 in mid-latitude regions. For instance, in Asia, the temperature contribution rose from 31% (1961–1990) to 36% (1991–2020), and similarly, in Europe from 28% to 38% (Fig. 7A,C,E). In contrast, North America and Africa showed relatively stable contributions throughout, dominated primarily by precipitation variability.

These results collectively indicate that while precipitation variability remains the dominant global driver of drought severity trends, the role of temperature-driven evaporative demand has strengthened significantly in recent decades, particularly in regions experiencing rapid warming. This growing temperature influence contributes meaningfully to observed increases in global drought synchrony, even without a corresponding increase in the spatial coherence of precipitation deficits.

Discussion

Concurrent and synchronized droughts pose significant risks to global food security, as simultaneous failures in key agricultural regions can severely disrupt food supply chains. Given the high probability of staple crop failure during moderate droughts, the potential for concurrent droughts could push global food systems to critical thresholds. Our findings indicate that although rising temperatures consistently amplify drought severity by increasing evaporative demand globally, regional variability in precipitation continues to constrain the extent of drought synchronization. Despite increasingly strong global teleconnections, the likelihood of large-scale simultaneous droughts on multiple continents remains lower than previously suggested [18]. Understanding this interplay between global climatic drivers and regional precipitation constraints is essential for informing effective resilience strategies in global food security, water resource management, and climate adaptation.

Our analysis explicitly quantifies the relative contributions of temperature and precipitation to drought severity trends. Approximately two-thirds of global drought severity changes are driven by precipitation variability, modulated substantially by sea surface temperature oscillations. Temperature-induced drying contributes the remaining one-third, with its influence notably increasing in mid-latitude regions experiencing rapid warming, such as Europe and Asia. This interplay between intensified evaporative demand from rising temperatures and persistent regional precipitation variability explains the observed increase in drought synchrony in recent decades, highlighting that while global drought synchrony is exacerbated by warming, its overall spatial extent remains constrained by precipitation dynamics.

The constrained global-scale synchronization implies that, despite significant localized drought risks, simultaneous crop failures across multiple major agricultural zones remain unlikely at present. However, the scenario in which regional droughts become increasingly synchronized and extensive, driven by intensified warming or altered precipitation patterns, could destabilize global food systems profoundly. Leveraging spatial variability in drought conditions—through strategic resource allocation and flexible trade policies—can thus provide critical buffers against global-scale disruptions.

Our findings open several important avenues for future investigation. While the self-calibrating Palmer Drought Severity Index (scPDSI) provided a consistent framework for evaluating drought dynamics at broad spatial and temporal scales, integrating alternative drought indices such as the Standardized Precipitation-Evapotranspiration Index (SPEI) could provide complementary insights into localized and short-term drought processes. Future work could also incorporate multiple observational datasets to test the sensitivity and generalizability of our conclusions, including alternative temperature (e.g., GISS, BEST), precipitation (e.g., GPCC), and sea surface temperature (SST) datasets (e.g., HadISST, Kaplan, COBE). Furthermore, incorporating direct soil moisture measurements and more detailed representations of vegetation and hydrological processes could further refine predictive models, enhancing the overall understanding of drought dynamics and synchronization under changing climate conditions.

Nevertheless, our findings significantly enhance understanding of global drought synchrony, explicitly clarifying the roles of temperature and precipitation. By identifying how large-scale climatic forcings interact with regional variability, we offer a clearer foundation for predictive modeling and strategic resilience planning. As climate change amplifies drought frequency and severity, strategically leveraging these insights will be critical for safeguarding agricultural stability, ensuring resilient food supply chains, and strengthening adaptive capacities globally.

Methods

Data

We use gridded monthly sc-PDSI data from 1901 to 2020 at a 0.5° x 0.5° spatial resolution, along with Temperature and precipitation available at the same spatial and temporal resolution obtained from the Climate Research Unit (CRU)[38, 39]. Additionally, we use the NOAA Extended Reconstructed SST V5 data, provided by NOAA PSL, Boulder, Colorado, USA, available at https://psl.noaa.gov/data/gridded/data.noaa.ersst.v5.html, on a 2.0° x 2.0° global grid resolution at a monthly scale. We used the Global Dataset of Historical Yield (GDHYv1.2+v1.3) that offers annual time series data of 0.5-degree grid-cell yield estimates of major crops worldwide for the period 1981-2016. The crops considered in this dataset are maize, rice, wheat and soybean [26]. We also utilize country-level annual crop yield (tons/hectare) data from 1961 to 2020, sourced from the Food and Agriculture Organization of the United Nations (FAO) Faostat statistical database (2019). Additionally, we use the MIRCA 2000 high-resolution global gridded dataset to obtain the total crop area for each crop [40].

Drought Onset and Drought Event

In this study, we define the onset of moderate drought using a threshold approach [15, 18, 19, 30], with a threshold of -2 based on the self-calibrating Palmer Drought Severity Index (sc-PDSI). We use the sc-PDSI due to its popularity as a drought indicator, given its use of the Penman–Monteith method for calculating potential evapotranspiration, which accounts for multiple climate variables and provides a more physically accurate representation of drought conditions. The sc-PDSI is widely recognized for global-scale drought analysis, particularly in the context of global warming, and has been extensively used in studies examining the impact of drought on ecosystems [38, 41, 42].

A drought onset is defined as the first month when the sc-PDSI value falls below this threshold, indicating the start of a moderate drought. Termination is defined as the time when the sc-PDSI value rises above the threshold. The duration of the drought is the period between its onset and termination. Each pair of drought onset and termination is counted as one drought event. We focus on moderate droughts to ensure that a sufficient number of events are captured at each location, providing a robust dataset for analysis.

Event Synchronization (ES)

Event Synchronization (ES) is a non-parametric method used to identify temporal dependencies between events, such as drought onsets. It captures the timing and delays between events without assuming linear relationships. In this study, ES is used to analyze drought onset synchronization across different regions, following the method described in [43–45].

The steps involved in the Event Synchronization approach are as follows:

- For two grid points, i and j, where drought events occur at times t_l^i and t_m^j, calculate the dynamic temporal delay, τ_{lm}^{ij}:

$$\tau_{lm}^{ij} = \min \left\{ \frac{t_{l+1}^i - t_l^i, t_l^i - t_{l-1}^i, t_{m+1}^j - t_m^j, t_m^j - t_{m-1}^j}{2} \right\} \tag{1}$$

  where s_i and s_j are the total number of drought events at grid points i and j, respectively. Two events are considered synchronized if the time gap between them does not exceed 3 months.
- Calculate the number of times an event at location i follows an event at location j, denoted $c(i|j)$:

$$c(i|j) = \sum_{l=1}^{s_i} \sum_{m=1}^{s_j} J_{ij} \tag{2}$$

  where:

$$J_{ij} = \begin{cases} 1 & \text{if } 0 < t_l^i - t_m^j < \tau_{lm}^{ij} \\ 0.50 & \text{if } t_l^i = t_m^j \\ 0 & \text{otherwise} \end{cases} \tag{3}$$

- The synchronization strength between grid points i and j is then calculated as:

$$Q_{ij} = \frac{c(i|j) + c(j|i)}{\sqrt{s_i s_j}} \tag{4}$$

- Once the ES computation is completed, a synchronization matrix is obtained with dimensions 59,721 x 59,721, representing the synchronization strength of drought onsets between all grid points globally.

Complex Network Analysis

Using the adjacency matrix obtained from the Event Synchronization (ES) analysis, we perform Complex Network (CN) analysis to study the synchronization of drought onsets across different regions. The steps involved in the CN analysis are as follows:

- Construct an undirected synchronization network where nodes represent grid locations and edges represent synchronization between two locations. Each edge indicates synchronization but does not imply direction.
- The adjacency matrix, A_{ij}^Q, is symmetric and contains synchronization values for all grid location pairs. We include only statistically significant connections by applying a threshold to the synchronization values. We set this threshold at the top 0.5% (99.5th quantile) of all non-zero synchronization values, denoted as θ.

- Convert the synchronization matrix into a binary adjacency matrix:

$$A_{ij}^{Q} = \begin{cases} 1 \text{ if} Q_{ij} > \theta \\ 0 \text{ otherwise} \end{cases} \tag{5}$$

Network Measures

To quantify the properties of the network, we use the following measures:

- **Degree Centrality (DC):** For a network with N nodes, the degree centrality of a node j measures the number of connections (edges) it has:

  $$\mathrm{DC}_j = \frac{\sum_{i=1}^{N-1} A_{ij}}{N-1} \tag{6}$$

  A high degree centrality indicates that the drought onset at grid point j is synchronized with many other locations.
- **Clustering Coefficient (CC):** The clustering coefficient CC_j of a node j measures how many of its neighbors are also connected to each other. It is calculated as:

  $$\mathrm{CC}_j = \frac{2\beta}{k_j(k_j-1)} \tag{7}$$

  where β is the number of actual connections between the neighbors of node j, and k_j is the number of neighbors of node j.
- **Average Link Length (ALL):** The average link length measures the average physical distance between connected nodes. It is computed as:

  $$\mathrm{ALL} = \frac{\sum_{i=1}^{N-1} A_{ij} d_{ij}}{\sum_{i=1}^{N-1} A_{ij}} \tag{8}$$

  where d_{ij} is the physical distance between grid points i and j.

Maximum Covariance Analysis

We use maximum covariance analysis (MCA) [31] to identify the coupled patterns of variability of sc-PDSI with sea surface temperature (SST) departure fields, obtained as the departure of each year's SST anomaly at each grid point from that year's global mean SST anomaly. Let X be $N_1 \times T$ (location $\times$ time), and Y be $N_2 \times T$ (location $\times$ time), representing the SST and sc-PDSI anomalies, respectively.

$$\frac{1}{T} XY^T = U\Sigma V^T \tag{9}$$

$$C = \frac{1}{T} XY^T$$

where C is the cross-correlation matrix. The orthonormal matrices U and V contain the spatial modes corresponding to the data fields X and Y respectively, and Σ is the diagonal matrix containing the singular values. The leading modes represent the main pattern of covariance between the two fields.

Time expansion coefficients, which represent how strongly each mode loads on each year, are given as:

$$T_{kU} = U_k^T X$$

$$T_{kV} = V_k^T Y$$

The squared covariance factor SCF_i is:

$$\mathrm{SCF}_i = \frac{\sigma_i^2}{\sum_j \sigma_j^2}$$

where σ_i is the i-th singular value and the denominator is the sum of the squares of all singular values.

Impact on Crop Yield

To assess the impact of droughts on crop yields, we used nationally averaged sc-PDSI values, where sc-PDSI ≤ -2 indicates moderate drought. Additionally, detrended crop yield data was employed to isolate the impact of climate-induced droughts on agricultural production. The crop yield data was detrended using the first difference (FD) method [46–48]:

$$\Delta\mathrm{Yield} = \mathrm{Yield}_i - \mathrm{Yield}_{i-1} \tag{10}$$

where ΔYield represents the detrended yield, Yield_i is the crop yield in year i, and Yield_{i-1} is the crop yield in the previous year.

Conditional Crop Failure Probability Estimation Based on Historical Data

To calculate the conditional probabilities of crop yield failure under drought conditions, we used empirical approach. For each grid point, we first identified all years where the sc-PDSI value during the growing season fell below -2 (indicating moderate drought). We then calculated the proportion of these years in which the crop yield fell below 0.5 times the standard deviation from the long-term mean yield. This proportion represents the conditional probability of crop failure, given the occurrence of a moderate drought. The calculation was performed for each crop across all available grid points. The conditional probability of crop yield failure under moderate drought conditions can be expressed as:

$$P(\text{Crop Failure} \mid \text{Drought}) = \frac{\sum_{i=1}^{n} I(\text{sc-PDSI}_i < -2 \land Y_i < \mu_Y - 0.5\sigma_Y)}{\sum_{i=1}^{n} I(\text{sc-PDSI}_i < -2)}$$

where:

- n is the number of years,
- $I(\cdot)$ is the indicator function, which equals 1 if the condition inside is true and 0 otherwise,
- sc-PDSI_i is the sc-PDSI value for year i,

- Y_i is the crop yield for year i,
- μ_Y is the long-term mean crop yield,
- σ_Y is the standard deviation of crop yield.

	Degree El Niño	**ALL El Niño**	**Degree La Niña**	**ALL La Niña**
Africa	119	6177	144	7112
Asia	119	3776	100	4310
Australia	732	6393	127	5120
North America	79	3507	98	4308
South America	201	5274	301	7096
Europe	111	4157	103	4377

Table 1: El Niño and La Niña Degrees and Average Link Length (ALL) by Continent.

Trend-partitioning experiments

To isolate and quantify the relative contributions of precipitation and temperature to drought severity trends, we employed the self-calibrating Palmer Drought Severity Index (scPDSI). Potential evapotranspiration (PET) was calculated using the Thornthwaite method [49], emphasizing temperature alone, with a fixed Available Water Capacity (AWC) of 100 mm assumed uniformly across all grid cells.

We generated three distinct scPDSI scenarios to explicitly partition precipitation and temperature influences:

1. **Observed run (OBS):**

$$\mathrm{scPDSI}_{\mathrm{OBS}} = f(P_{\mathrm{obs}}, \mathrm{PET}_{\mathrm{obs}}) \tag{11}$$

2. **Fixed-Precipitation run (P-CLIM):**

$$\mathrm{scPDSI}_{\mathrm{P-CLIM}} = f(\overline{P}_{\mathrm{clim}}, \mathrm{PET}_{\mathrm{obs}}) \tag{12}$$

3. **Fixed-PET run (PET-CLIM):**

$$\mathrm{scPDSI}_{\mathrm{PET-CLIM}} = f(P_{\mathrm{obs}}, \overline{\mathrm{PET}}_{\mathrm{clim}}) \tag{13}$$

Here, P_{obs} and $\mathrm{PET}_{\mathrm{obs}}$ represent observed monthly precipitation and potential evapotranspiration, respectively, from CRU TS v4.07 (1901–2021). $\overline{P}_{\mathrm{clim}}$ and $\overline{\mathrm{PET}}_{\mathrm{clim}}$ indicate monthly climatological averages computed over the entire analysis period (1901–2021).

Linear trends were calculated using the non-parametric Sen's slope estimator [**?**] applied separately to monthly scPDSI values for two distinct 31-year periods: 1961–1990 and 1991–2020. Monthly trend values were converted to annual trends by scaling with a factor of 12:

$$\text{Annual trend} = 12 \times (\text{monthly Sen's slope}) \tag{14}$$

The fractional contributions of precipitation (F_P) and temperature-driven evapotranspiration (F_T) to the observed drought severity trends were quantified using the differences between the observed trends and those from the sensitivity experiments:

$$F_P = \frac{|\mathrm{Trend}_{\mathrm{OBS}} - \mathrm{Trend}_{\mathrm{P-CLIM}}|}{|\mathrm{Trend}_{\mathrm{OBS}}|} \times 100\% \tag{15}$$

$$F_T = \frac{|\mathrm{Trend}_{\mathrm{OBS}} - \mathrm{Trend}_{\mathrm{PET-CLIM}}|}{|\mathrm{Trend}_{\mathrm{OBS}}|} \times 100\% \tag{16}$$

Spatial patterns and regional summaries of these fractional contributions are presented in the main text (Fig. 7).

Code availability

Python scripts for the analysis and figures are publicly available on GitHub (https://github.com/Drought-JohnDoe/Drought-JohnDoe). We use the climate_indices [50] package in python to calculate PET using Thornthwaite method and scPDSI.

Competing interests

The authors declare no conflict of interest.

Acknowledgment

References

[1] Mishra, A. K. & Singh, V. P. A review of drought concepts. Journal of hydrology **391**, 202–216 (2010).

[2] Andreadis, K. M., Clark, E. A., Wood, A. W., Hamlet, A. F. & Lettenmaier, D. P. Twentieth-century drought in the conterminous united states. Journal of Hydrometeorology **6**, 985–1001 (2005).

[3] Herrera-Estrada, J. E., Satoh, Y. & Sheffield, J. Spatiotemporal dynamics of global drought. Geophysical Research Letters **44**, 2254–2263 (2017).

[4] Konapala, G. & Mishra, A. Review of complex networks application in hydroclimatic extremes with an implementation to characterize spatio-temporal drought propagation in continental usa. Journal of Hydrology **555**, 600–620 (2017).

[5] Mehrabi, Z. & Ramankutty, N. Synchronized failure of global crop production. Nature Ecology and Evolution **3**, 780–786 (2019).

[6] Gaupp, F., Hall, J., Hochrainer-Stigler, S. & Dadson, S. Changing risks of simultaneous global breadbasket failure. Nature Climate Change **10**, 54–57 (2020).

[7] Dai, A. Drought under global warming: a review. Wiley Interdisciplinary Reviews: Climate Change **2**, 45–65 (2011).

[8] Von Braun, J. & Tadesse, G. Global food price volatility and spikes: an overview of costs, causes, and solutions. ZEF-Discussion Papers on Development Policy (2012).

[9] Sarhadi, A., Ausín, M. C., Wiper, M. P., Touma, D. & Diffenbaugh, N. S. Multidimensional risk in a nonstationary climate: Joint probability of increasingly severe warm and dry conditions. Science advances **4**, eaau3487 (2018).

[10] Tigchelaar, M., Battisti, D. S., Naylor, R. L. & Ray, D. K. Future warming increases probability of globally synchronized maize production shocks. Proceedings of the National Academy of Sciences **115**, 6644–6649 (2018).

[11] Zhou, P. & Liu, Z. Likelihood of concurrent climate extremes and variations over china. Environmental Research Letters **13**, 094023 (2018).

[12] Raymond, C. et al. Understanding and managing connected extreme events. Nature climate change **10**, 611–621 (2020).

[13] Mondal, S., Mishra, A. K. & Leung, L. R. Spatiotemporal characteristics and propagation of summer extreme precipitation events over united states: A complex network analysis. Geophysical Research Letters **47**, e2020GL088185 (2020).

[14] Boers, N., Bookhagen, B., Marwan, N., Kurths, J. & Marengo, J. Complex networks identify spatial patterns of extreme rainfall events of the south american monsoon system. Geophysical Research Letters **40**, 4386–4392 (2013).

[15] Mondal, S. & Mishra, A. K. Complex networks reveal heatwave patterns and propagations over the usa (2021).

[16] Tantary, D. et al. Geographical trapping of synchronous extremes amidst increasing variability of indian summer monsoon rainfall. Geophysical Research Letters **50**, e2023GL104788 (2023).

[17] Kornhuber, K. et al. Extreme weather events in early summer 2018 connected by a recurrent hemispheric wave-7 pattern. Environmental Research Letters **14**, 054002 (2019).

[18] Mondal, S., Mishra, A. K., Leung, R. & Cook, B. Global droughts connected by linkages between drought hubs. Nature Communications **14** (2023).

[19] Chauhan, T., Chandel, V. & Ghosh, S. Global land drought hubs confounded by teleconnection hotspots in equatorial oceans. npj Climate and Atmospheric Science **7** (2024).

[20] Mishra, V., Smoliak, B. V., Lettenmaier, D. P. & Wallace, J. M. A prominent pattern of year-to-year variability in indian summer monsoon rainfall. Proceedings of the National Academy of Sciences **109**, 7213–7217 (2012).

[21] Feng, S., Hu, Q. & Oglesby, R. J. Influence of atlantic sea surface temperatures on persistent drought in north america. Climate Dynamics **37**, 569–586 (2011).

[22] Chen, X. & Tung, K.-K. Global-mean surface temperature variability: Space–time perspective from rotated eofs. Climate Dynamics **51**, 1719–1732 (2018).

[23] Donges, J. F., Petrova, I., Loew, A., Marwan, N. & Kurths, J. How complex climate networks complement eigen techniques for the statistical analysis of climatological data. Climate Dynamics **45**, 2407–2424 (2015).

[24] Sheffield, J., Wood, E. F. & Roderick, M. L. Little change in global drought over the past 60 years. Nature **491**, 435–438 (2012).

[25] Dai, A. Increasing drought under global warming in observations and models. Nature climate change **3**, 52–58 (2013).

[26] Iizumi, T. Global dataset of historical yields v1.2 and v1.3 aligned version (2019). URL https://doi.org/10.1594/PANGAEA.909132. Supplement to: Iizumi, Toshichika; Sakai, T (2020): The global dataset of historical yields for major crops 1981–2016. Scientific Data, 7(1), 97, https://doi.org/10.1038/s41597-020-0433-7.

[27] Boers, N. et al. Complex networks reveal global pattern of extreme-rainfall teleconnections. Nature **566**, 373–377 (2019).

[28] Reason, C. The bolivian, botswana, and bilybara highs and southern hemisphere drought/floods. Geophysical Research Letters **43**, 1280–1286 (2016).

[29] Singh, J. et al. Enhanced risk of concurrent regional droughts with increased enso variability and warming. Nature Climate Change **12**, 163–170 (2022).

[30] Mondal, S., Mishra, A. K. & Leung, L. R. Spatiotemporal characteristics and propagation of summer extreme precipitation events over united states: A complex network analysis. Geophysical Research Letters **47** (2020).

[31] Bretherton, C. S., Smith, C. & Wallace, J. M. An intercomparison of methods for finding coupled patterns in climate data. Journal of climate **5**, 541–560 (1992).

[32] Anderson, W., Seager, R., Baethgen, W., Cane, M. & You, L. Synchronous crop failures and climate-forced production variability. Science advances **5**, eaaw1976 (2019).

[33] Cai, W. et al. Climate impacts of the el niño–southern oscillation on south america (2020).

[34] Athira, K. et al. Regional and temporal variability of indian summer monsoon rainfall in relation to el niño southern oscillation. Scientific Reports **13**, 12643 (2023).

[35] Wallace, J. M. & Gutzler, D. S. Teleconnections in the geopotential height field during the northern hemisphere winter. Monthly weather review **109**, 784–812 (1981).

[36] Hurrell, J. W. Decadal trends in the north atlantic oscillation: Regional temperatures and precipitation. Science **269**, 676–679 (1995).

[37] Wells, N., Goddard, S. & Hayes, M. J. A self-calibrating palmer drought severity index. Journal of climate **17**, 2335–2351 (2004).

[38] van der Schrier, G., Barichivich, J., Briffa, K. & Jones, P. A scpdsi-based global data set of dry and wet spells for 1901–2009. Journal of Geophysical Research: Atmospheres **118**, 4025–4048 (2013).

[39] Harris, I., Osborn, T. J., Jones, P. & Lister, D. Version 4 of the cru ts monthly high-resolution gridded multivariate climate dataset. Scientific data **7**, 109 (2020).

[40] Portmann, F. T., Siebert, S. & Döll, P. Mirca2000—global monthly irrigated and rainfed crop areas around the year 2000: A new high-resolution data set for agricultural and hydrological modeling. Global biogeochemical cycles **24** (2010).

[41] Wang, Q. et al. Assessing the impacts of drought on grassland net primary production at the global scale. Scientific reports **9**, 14041 (2019).

[42] Pandžić, K. et al. Application of the self-calibrated palmer drought severity index and standardized precipitation index for estimation of drought impact on maize grain yield in pannonian part of croatia. Natural hazards **113**, 1237–1262 (2022).

[43] Boers, N., Bookhagen, B., Marwan, N., Kurths, J. & Marengo, J. Complex networks identify spatial patterns of extreme rainfall events of the south american monsoon system. Geophysical Research Letters **40**, 4386–4392 (2013).

[44] Boers, N. et al. Complex networks reveal global pattern of extreme-rainfall teleconnections. Nature **566**, 373–377 (2019).

[45] Malik, N., Bookhagen, B., Marwan, N. & Kurths, J. Analysis of spatial and temporal extreme monsoonal rainfall over south asia using complex networks. Climate Dynamics **39**, 971–987 (2012).

[46] Tao, F., Yokozawa, M., Liu, J. & Zhang, Z. Climate–crop yield relationships at provincial scales in china and the impacts of recent climate trends. Climate Research **38**, 83–94 (2008).

[47] Zhang, T., Zhu, J. & Wassmann, R. Responses of rice yields to recent climate change in china: An empirical assessment based on long-term observations at different spatial scales (1981–2005). Agricultural and Forest Meteorology **150**, 1128–1137 (2010).

[48] Wang, B. et al. Effects of climate trends and variability on wheat yield variability in eastern australia. Climate Research **64**, 173–186 (2015).

[49] Thornthwaite, C. W. An approach toward a rational classification of climate. Geographical review **38**, 55–94 (1948).

[50] Adams, J. climate_indices: An open source python library providing reference implementations of commonly used climate indices. https://github.com/monocongo/climate_indices (2017). Accessed: July 10, 2025.

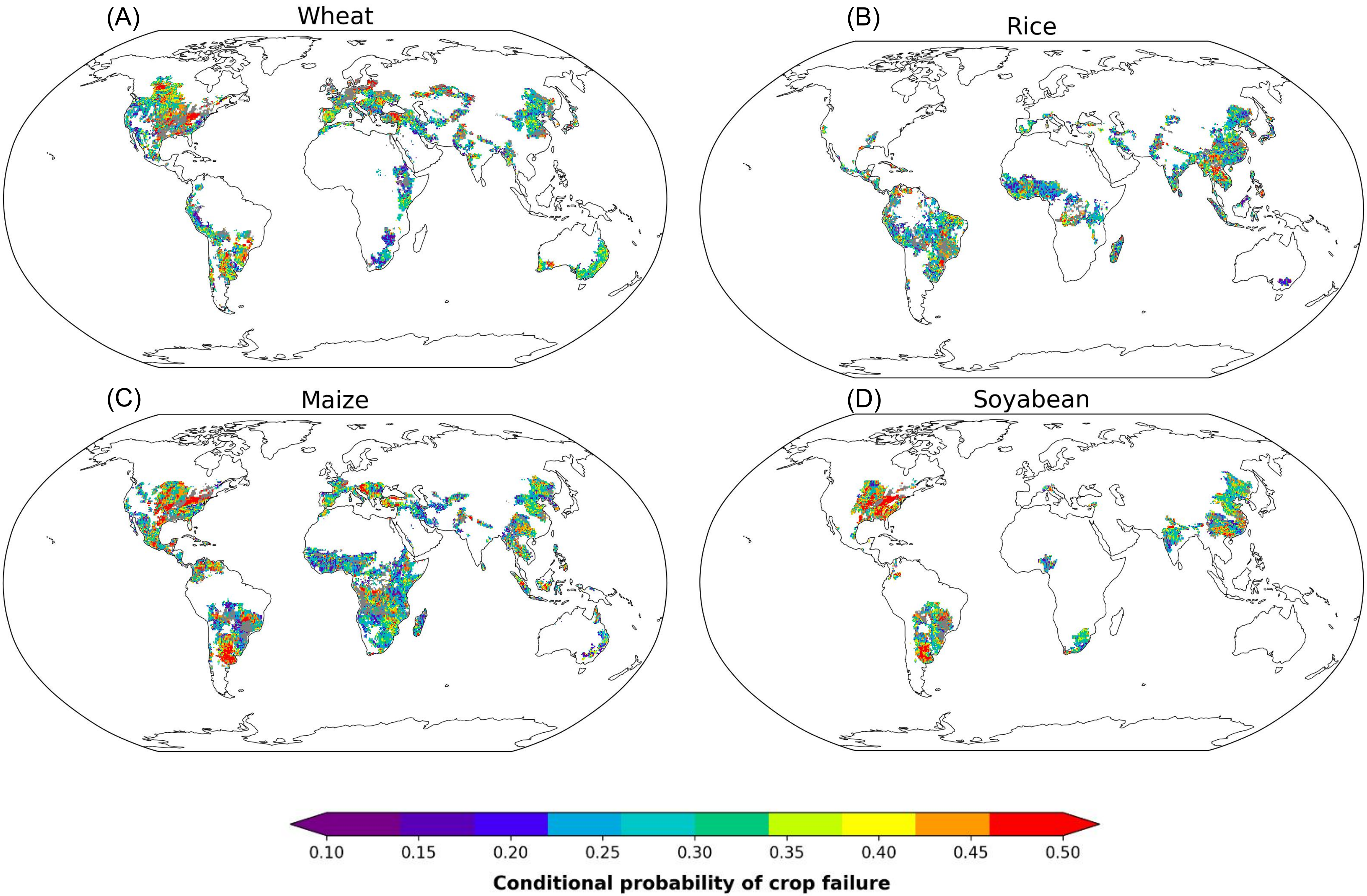
(A)
Wheat
(B)
Rice
(C)
Maize
(D)
Soyabean
0.10
0.15
0.20
0.25
0.30
0.35
0.40
0.45
0.50
Conditional probability of crop failure

Fig. 1: Conditional probability of crop yield failure and moderate drought across key global regions. Conditional probability of crop yield failure and moderate drought conditions for (A) Wheat, (B) Rice, (C) Maize, and (D) Soybean. Each panel shows the probability of yield falling below 0.5 standard deviation of long term mean (indicative of yield failure) and sc-PDSI values below -2, indicating moderate drought. Maize and Soybean exhibit the highest failure probability across the North and South America. Grey color indicate zero probabilities and white color represents no data available (non cropland). Most nations show at least one crop with a significant probability of failure when moderate droughts occur.(see Methods).

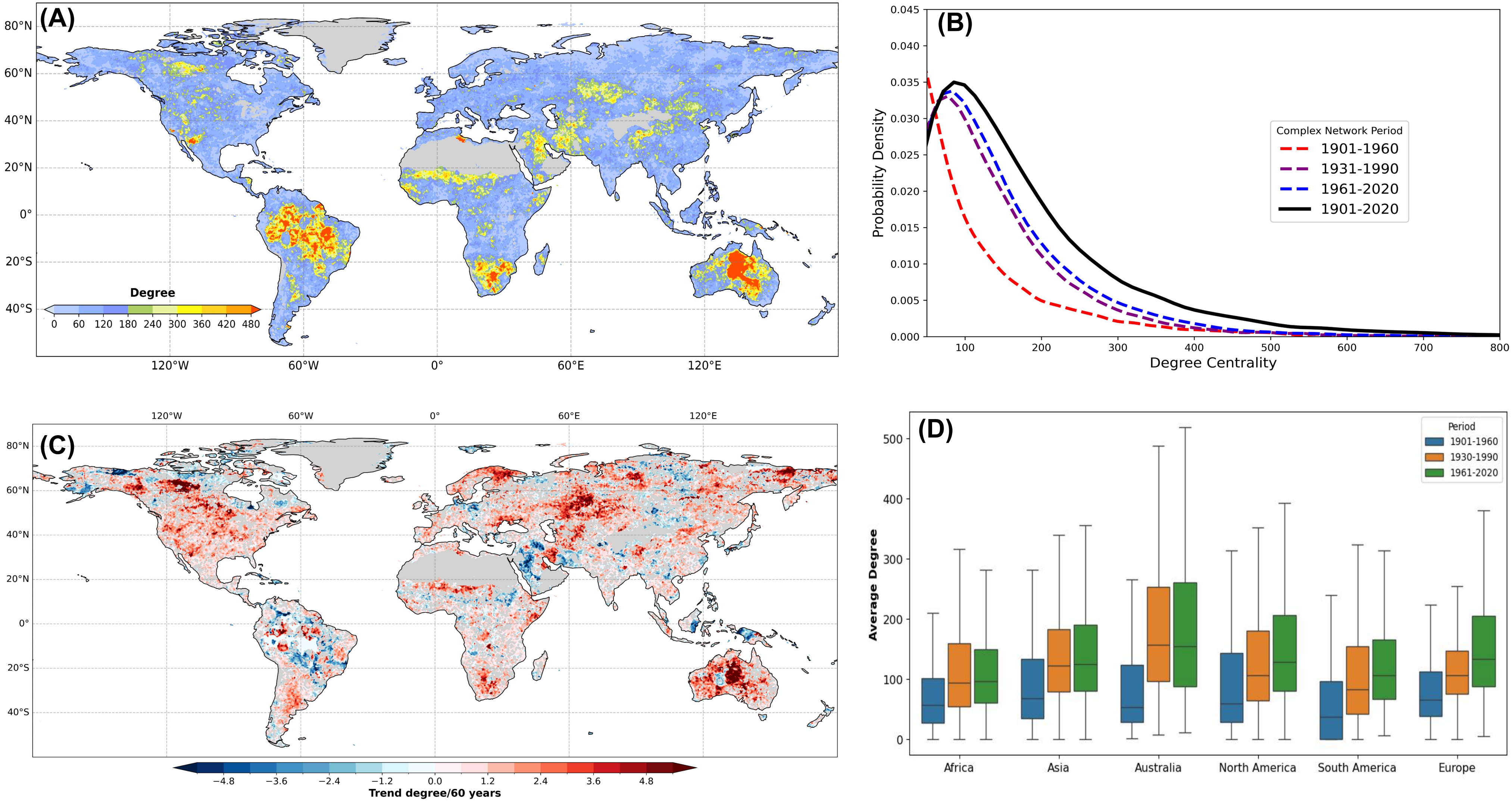
(A)
80°N
60°N
40°N
20°N
0°
20°S
40°S
120°W
60°W
0°
60°E
120°E
Degree
0 60 120 180 240 300 360 420 480
(B)
Probability Density
0.045
0.040
0.035
0.030
0.025
0.020
0.015
0.010
0.005
0.000
Complex Network Period
1901-1960
1931-1990
1961-2020
1901-2020
100 200 300 400 500 600 700 800
Degree Centrality
(C)
Trend degree/60 years
−4.8 −3.6 −2.4 −1.2 0.0 1.2 2.4 3.6 4.8
(D)
Average Degree
0 100 200 300 400 500
Period
1901-1960
1930-1990
1961-2020
Africa
Asia
Australia
North America
South America
Europe

Fig. 2: Spatial connectivity structure of global droughts. **(A)** Degree centrality of the global drought network, illustrating areas of high spatial clustering. **(B)** Degree distribution across different time periods, showing a heavy tail indicative of drought hubs. **(C)** Temporal trends in degree centrality (1901–2020), identified via the Mann-Kendall test ($p < 0.05$). **(D)** Box plot of degree centrality for continents across three periods, showing Australia with the highest degree.

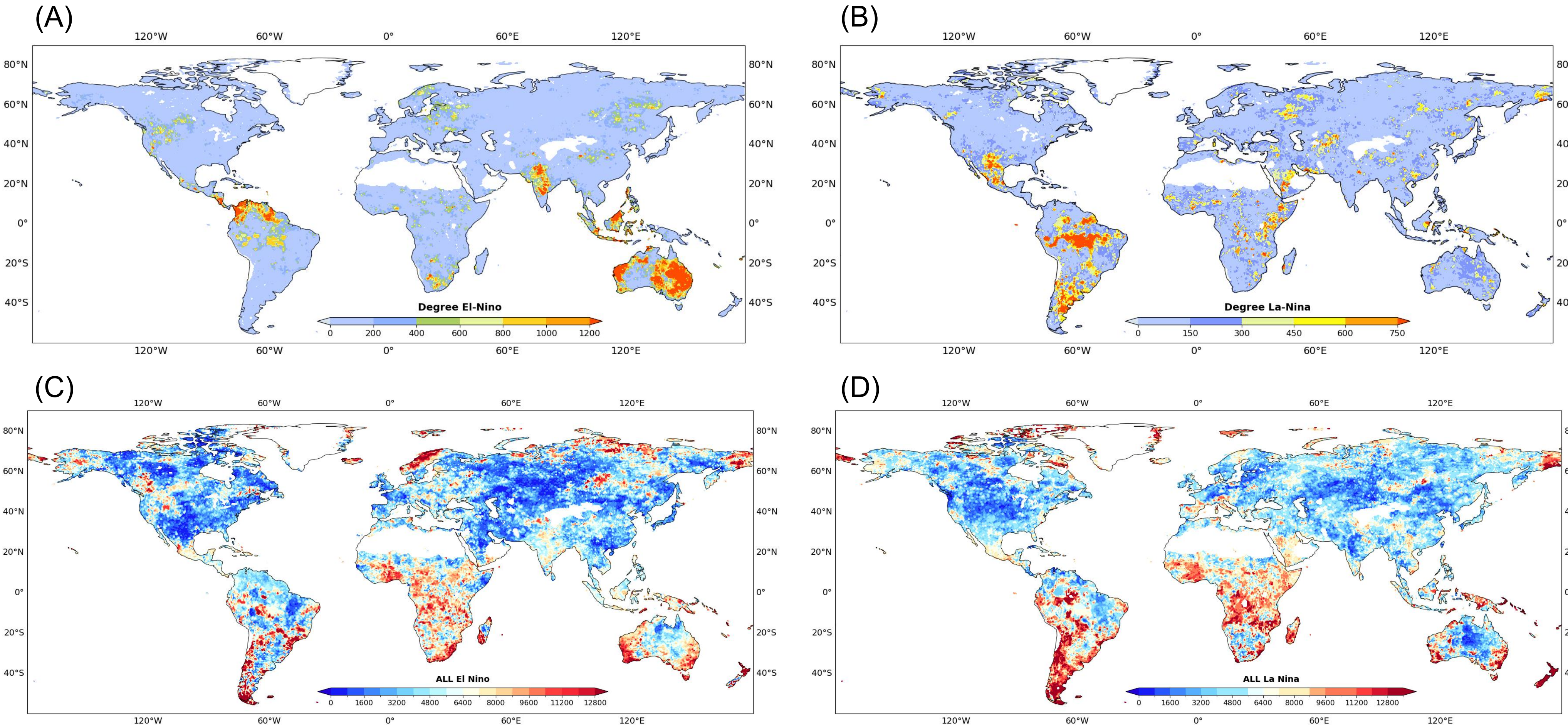
(A)
120°W
60°W
0°
60°E
120°E
80°N
60°N
40°N
20°N
0°
20°S
40°S
Degree El-Nino
0
200
400
600
800
1000
1200
(B)
Degree La-Nina
0
150
300
450
600
750
(C)
ALL El Nino
0
1600
3200
4800
6400
8000
9600
11200
12800
(D)
ALL La Nina

Fig. 3: Spatial connectivity structure and spread of global droughts during ENSO positive and Negative Periods. **(A)** and **(C)** Degree Centrality and Average Link Length of the complex network formed using El Niño years **(B)** and **(D)** La Niña years respectively.

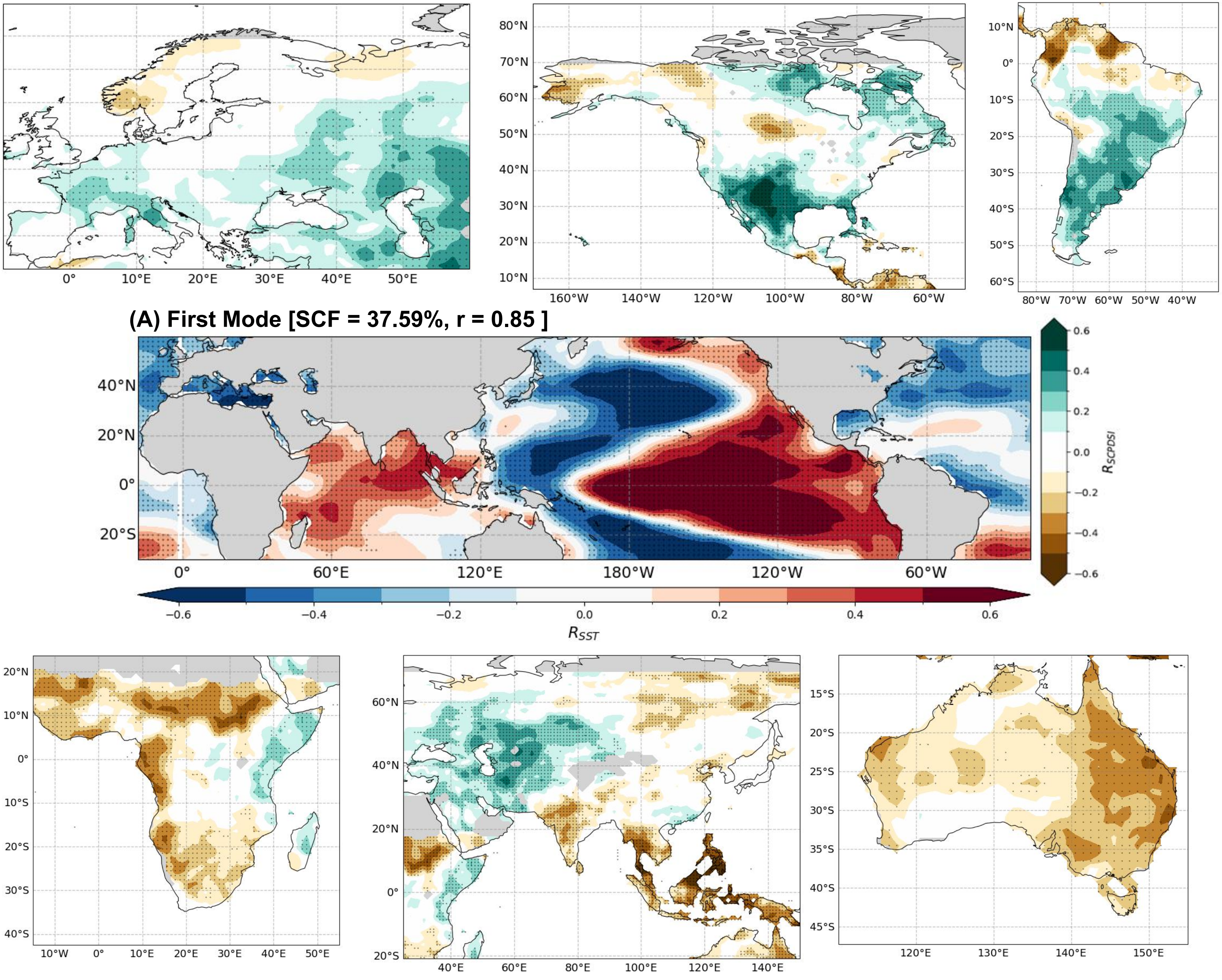
(A) First Mode [SCF = 37.59%, r = 0.85]

Fig. 4: Coupled pattern analysis of sc-PDSI and SST anomalies. (A) Heterogeneous correlation coefficients between sc-PDSI expansion coefficients and SST anomalies (1901–2020) for the first and second leading modes. All correlations are significant at $p < 0.05$.

(A) First Mode (1901-1960) [SCF = 32 %, r = 0.87]

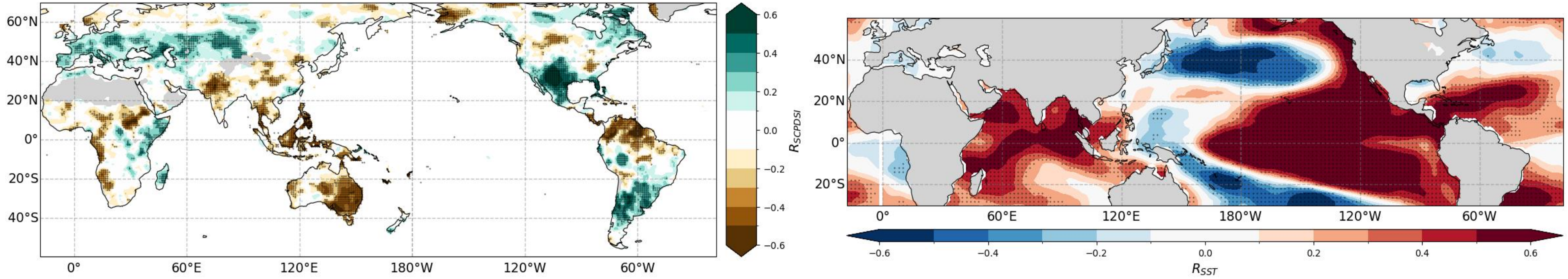

(B) First Mode (1961-2020) [SCF = 38.8 %, r = 0.86]

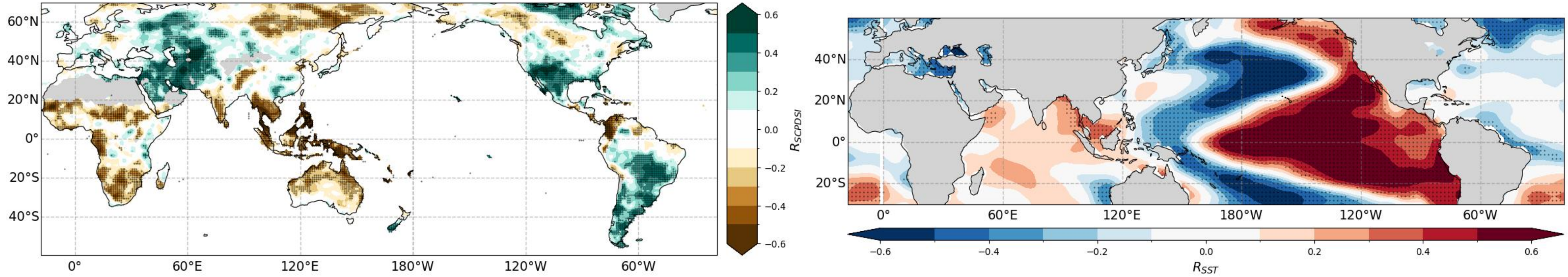

(C) Difference

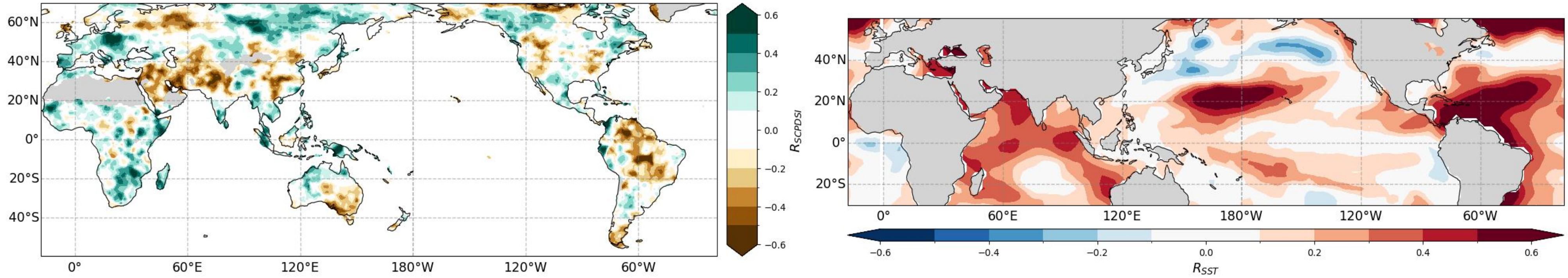

Fig. 5: Comparison of MCA analysis of sc-PDSI and SST anomalies between two periods (1901–1960 and 1961–2020). (A) Leading mode during 1901–1960, showing heterogeneous correlation coefficients between SST PC1 and sc-PDSI over land, and sc-PDSI PC1 and SST anomalies over oceans. **(B)** Same as (A), but for 1961–2020. **(C)** Difference in leading modes between the two periods (1961–2020 minus 1901–1960).

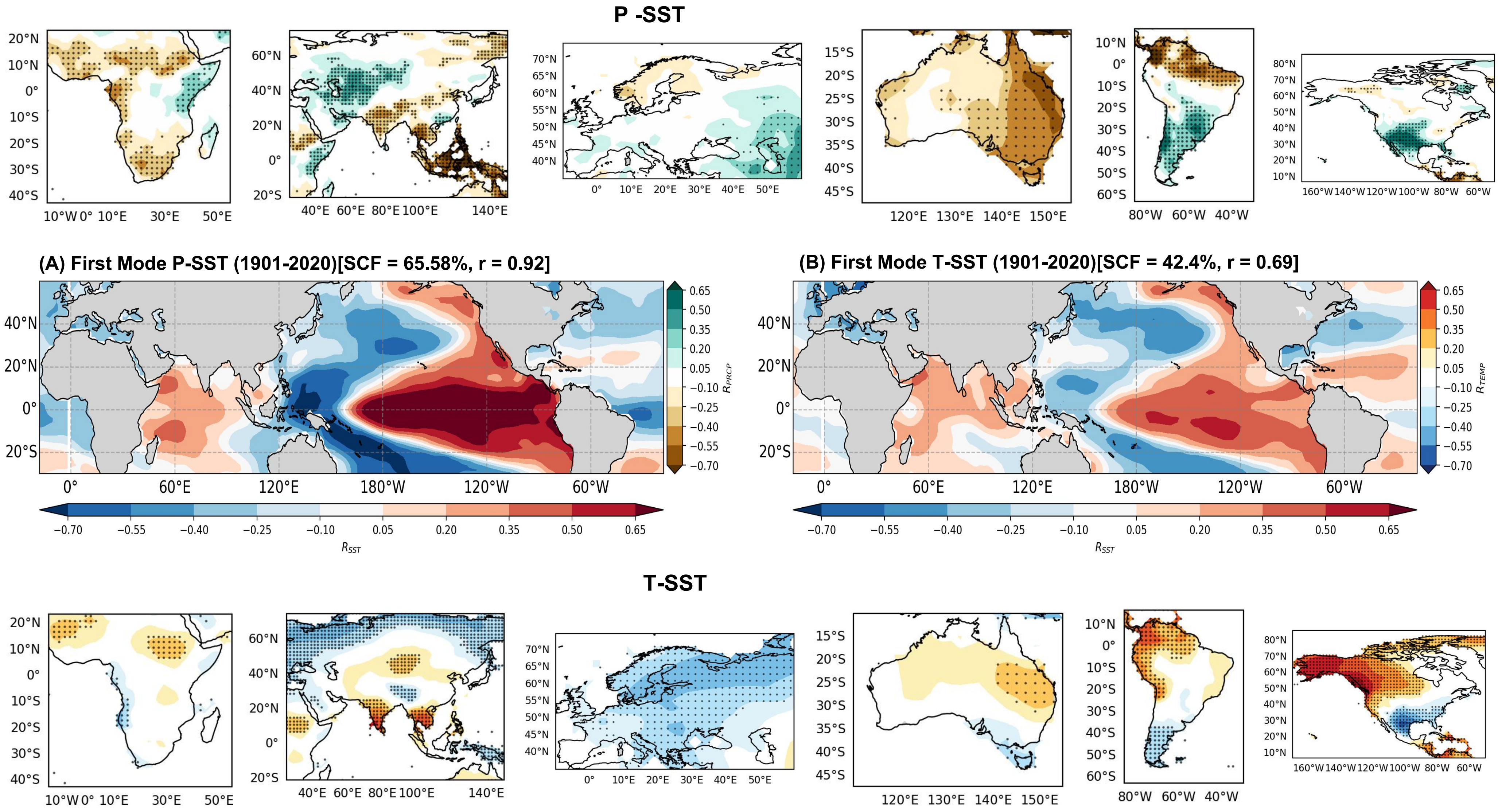
P -SST

(A) First Mode P-SST (1901-2020)[SCF = 65.58%, r = 0.92]

(B) First Mode T-SST (1901-2020)[SCF = 42.4%, r = 0.69]

T-SST

Fig. 6: First leading modes of variability of precipitation (P) and temperature (T) with anomalies in sea surface temperature (SST). (A) The first mode of P-SST variability explains 65.6% of the squared covariance fraction (SCF) and resembles the ENSO pattern, with SST anomalies in the equatorial Pacific showing opposite signs to precipitation anomalies in Australia, Southeast Asia, and Africa ($r = 0.92$, $p < 0.05$). **(B)** The first mode of T-SST variability explains 42.4% of the squared covariance fraction ($r = 0.69$, $p < 0.05$), with the dominant influence of global warming removed from global temperature fields.

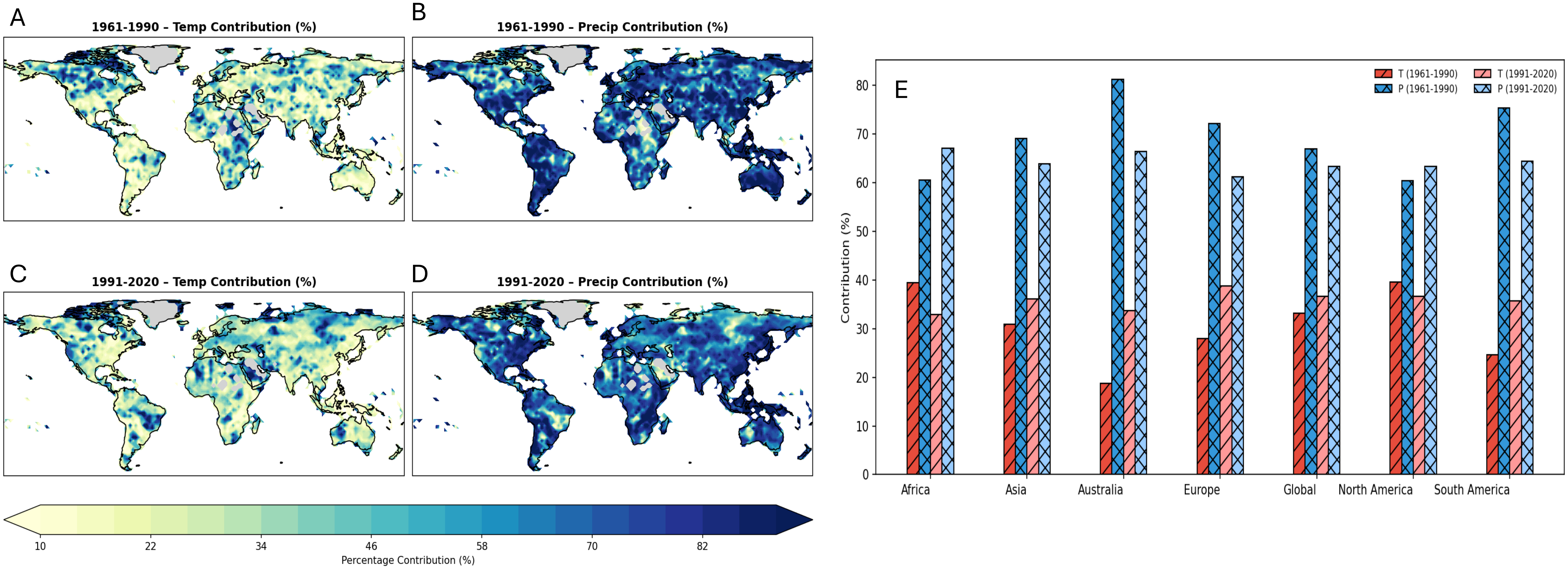
A
1961-1990 – Temp Contribution (%)
B
1961-1990 – Precip Contribution (%)
C
1991-2020 – Temp Contribution (%)
D
1991-2020 – Precip Contribution (%)
10
22
34
46
58
70
82
Percentage Contribution (%)
E
T (1961-1990)
P (1961-1990)
T (1991-2020)
P (1991-2020)
Contribution (%)
0
10
20
30
40
50
60
70
80
Africa
Asia
Australia
Europe
Global
North America
South America

Fig. 7: Spatial and regional contributions of temperature-driven PET and precipitation to observed scPDSI trends. Panels **A-D** show the percentage contribution of temperature and precipitation to observed changes in monthly self-calibrating PDSI (scPDSI) over two periods: 1961–1990 (A–B) and 1991–2020 (C–D). PET was computed using the Thornthwaite method to isolate the role of temperature alone. Contributions are calculated by comparing scPDSI trends from the observed simulation to two sensitivity experiments: one where precipitation is held fixed at its 1961–1990 climatology (P-CLIM) and another where PET is held fixed (PET-CLIM).Panel E summarizes the regional and global average contributions of temperature and precipitation across continents for both time periods These trends are influenced by the evolving balance between temperature-driven evaporative demand and precipitation variability, with the role of temperature increasing after 1990, especially in the mid-latitudes, but precipitation remains the dominant driver globally.

Supplementary Information

Oceanic Variability and its Regional Responses Limit the Extent of Global Drought Synchrony

This file includes:

Methods
Supplementary Figures S1 to S9
Supplementary Table 1 to 4

Methods

Copula Method For joint probability Of crop Failure assessment

To assess the impact of droughts on crop yields, we used nationally averaged sc-PDSI values, where sc-PDSI ≤ -2 indicates moderate drought. Additionally, detrended crop yield data was employed to isolate the impact of climate-induced droughts on agricultural production. The crop yield data was detrended using the first difference (FD) method:

$$\mathbf{\Delta Yield = Yield_i - Yield_{i-1}}$$

where **ΔYield** represents the detrended yield, $\mathbf{Yield_i}$ is the crop yield in year **i**, and $\mathbf{Yield_{i-1}}$ is the crop yield in the previous year. This detrending process removes long-term trends from the data associated with technological advancements and other influences, allowing us to focus on climate variability. The analysis spans the period from 1962 to 2020 using the yield data provided by FAO.

To model the dependence between nationally averaged sc-PDSI values (X) and detrended crop yields (Y), we employed a copula-based approach, which allows the separation of marginal distributions from the dependence structure.

The joint cumulative distribution function (CDF) of sc-PDSI and crop yield, $\mathbf{F_{X,Y}(x, y)}$, can be decomposed using Sklar's Theorem into the marginal CDFs, $\mathbf{F_X(x)}$ and $\mathbf{F_Y(y)}$, and a copula C, which captures the dependency structure:

$$\mathbf{F_{X,Y}(x, y) = C(F_X(x), F_Y(y))}$$

where C(u, v) is the copula function, with $u = F_X(x)$ and $v = F_Y(y)$ representing the marginal CDFs of sc-PDSI and crop yield, respectively. The copula function C provides the joint distribution of these variables independent of their marginals.

We used a parametric bootstrapping goodness-of-fit test to select the best-fitting copula for each country, determining the optimal copula by minimizing the test statistic (Genest et al., 2008; Sadegh et al., 2017).

Calculating Probability of Crop Failure

After selecting the best-fitting copula, we computed the conditional probability of crop yield failure, given moderate drought conditions ($X \leq -2$). Crop failure is defined as the yield falling below a critical threshold, Y_{thr}, which is one standard deviation below the long-term mean yield.

$$\mathbf{P(y \leq Y_{thr} \mid x \leq -2) = C[F_X(-2), F_Y(Y_{thr})] / F_X(-2)}$$

This equation provides the conditional probability that the crop yield falls below the threshold Y_{thr}, given that sc-PDSI (X) is less than or equal to -2 (moderate drought).

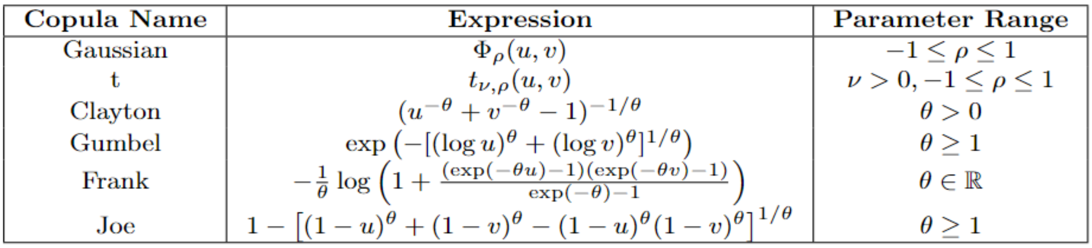

Copula Name	Expression	Parameter Range
Gaussian	$\Phi_\rho(u, v)$	$-1 \leq \rho \leq 1$
t	$t_{\nu,\rho}(u, v)$	$\nu > 0, -1 \leq \rho \leq 1$
Clayton	$(u^{-\theta} + v^{-\theta} - 1)^{-1/\theta}$	$\theta > 0$
Gumbel	$\exp\left(-[(\log u)^\theta + (\log v)^\theta]^{1/\theta}\right)$	$\theta \geq 1$
Frank	$-\frac{1}{\theta} \log\left(1 + \frac{(\exp(-\theta u)-1)(\exp(-\theta v)-1)}{\exp(-\theta)-1}\right)$	$\theta \in \mathbb{R}$
Joe	$1 - \left[(1-u)^\theta + (1-v)^\theta - (1-u)^\theta (1-v)^\theta\right]^{1/\theta}$	$\theta \geq 1$

Table 1: List of copula distributions with their expressions and parameter ranges.

(A)

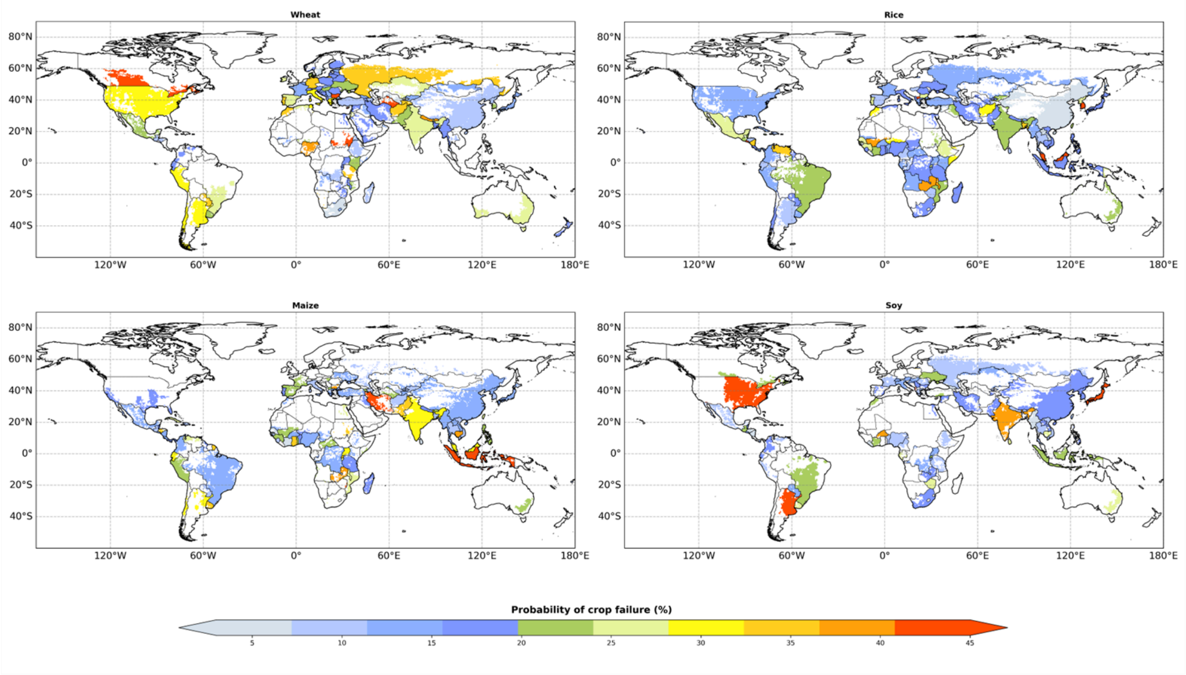

(B)

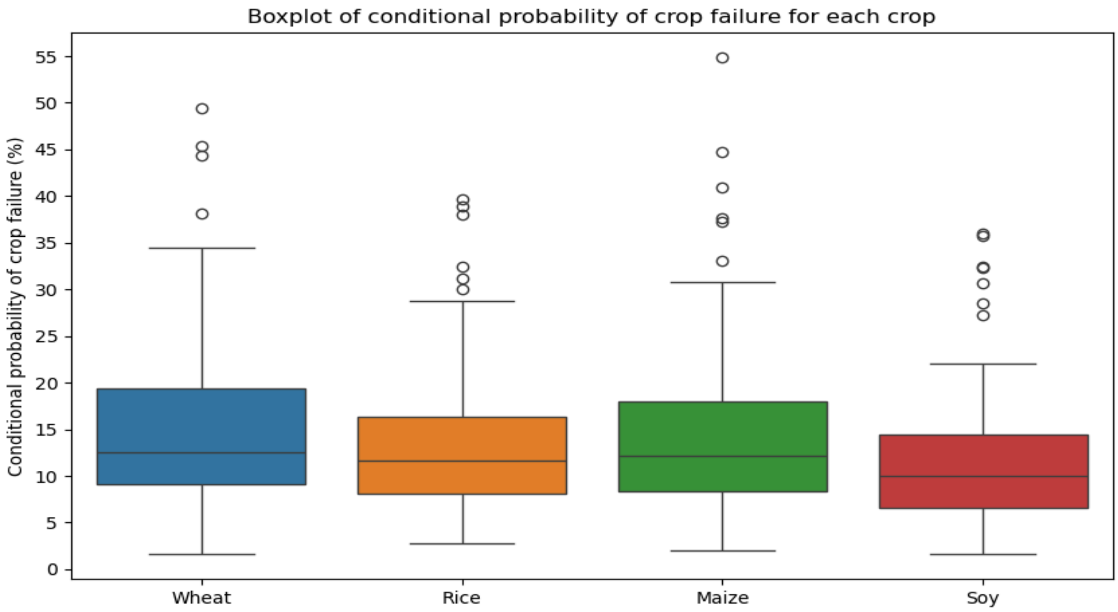

Supplementary Figure S1

- **A.** Conditional probability of crop failure (yield below mean- 1*std). Given that the sc-PDSI is below a certain threshold of -2 indicative of moderate drought conditions calculated using the best fit bivariate copula.
- **B.** Box plot for conditional probability of crop failure for staple cereal crops across different countries.

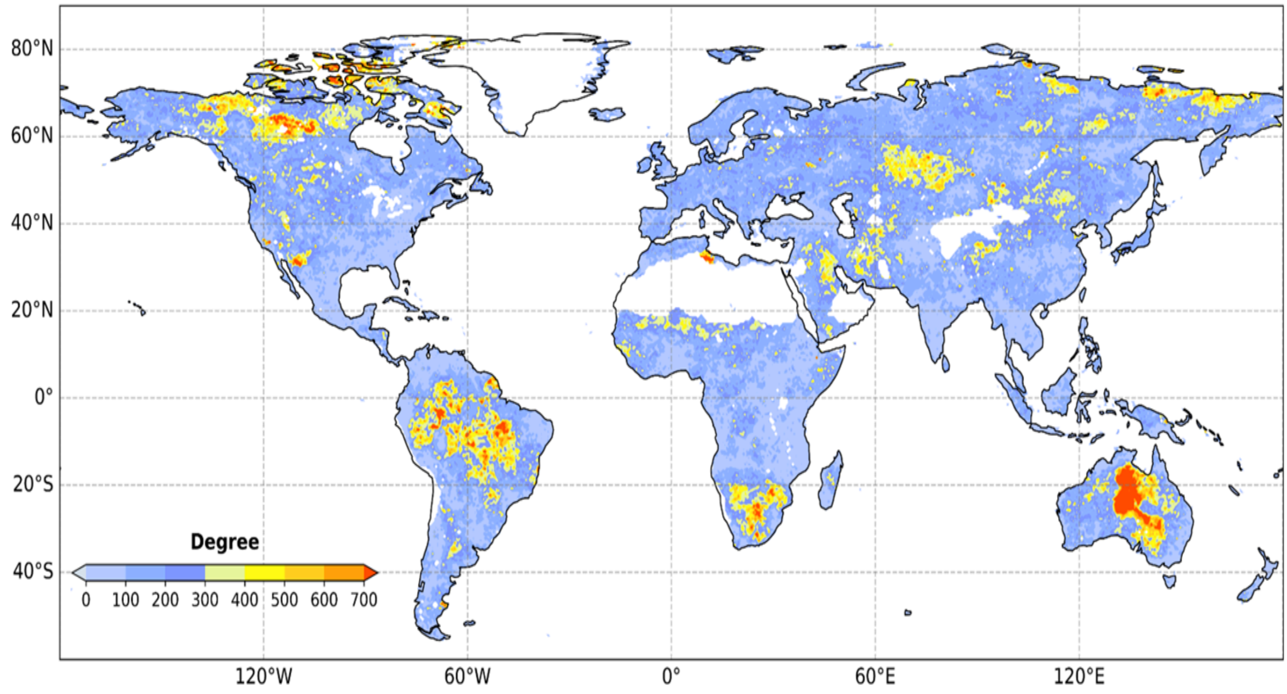

Supplementary Figure S2 Degree Centrality of complex network formed by ES on drought onset (1901-2020) without correction against projection system (original).

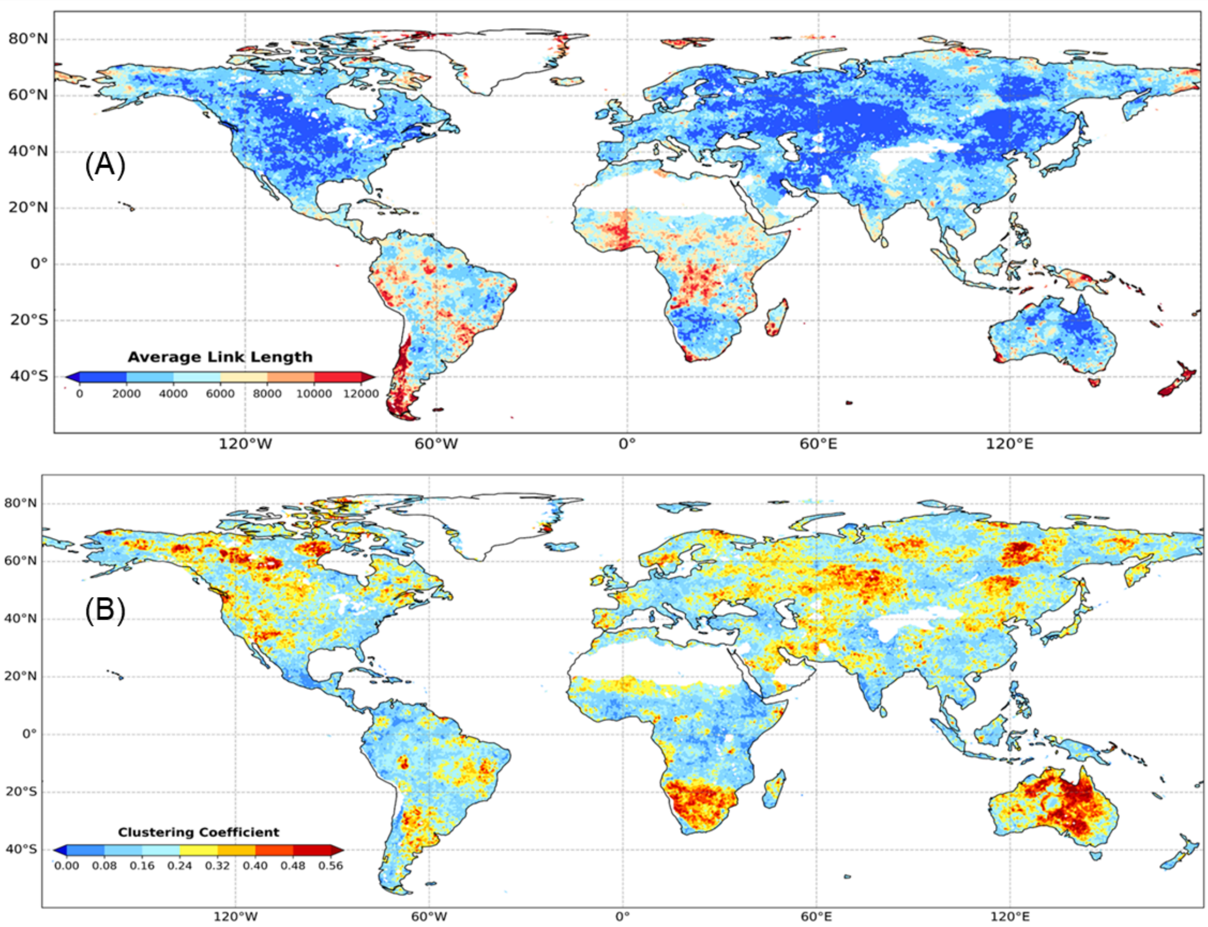

Supplementary Figure S3 Regional and Spatial extent of network connections.
(A) Average Link length for the drought network in the period 1901-2020 with South America having the farthest connections.
(B) The Local Clustering Coefficient (LCC) for the period 1901-2020 shows the regional interconnectivity between a grid's neighbors.Australia and Africa have very dense interconnectivity between neighbors.

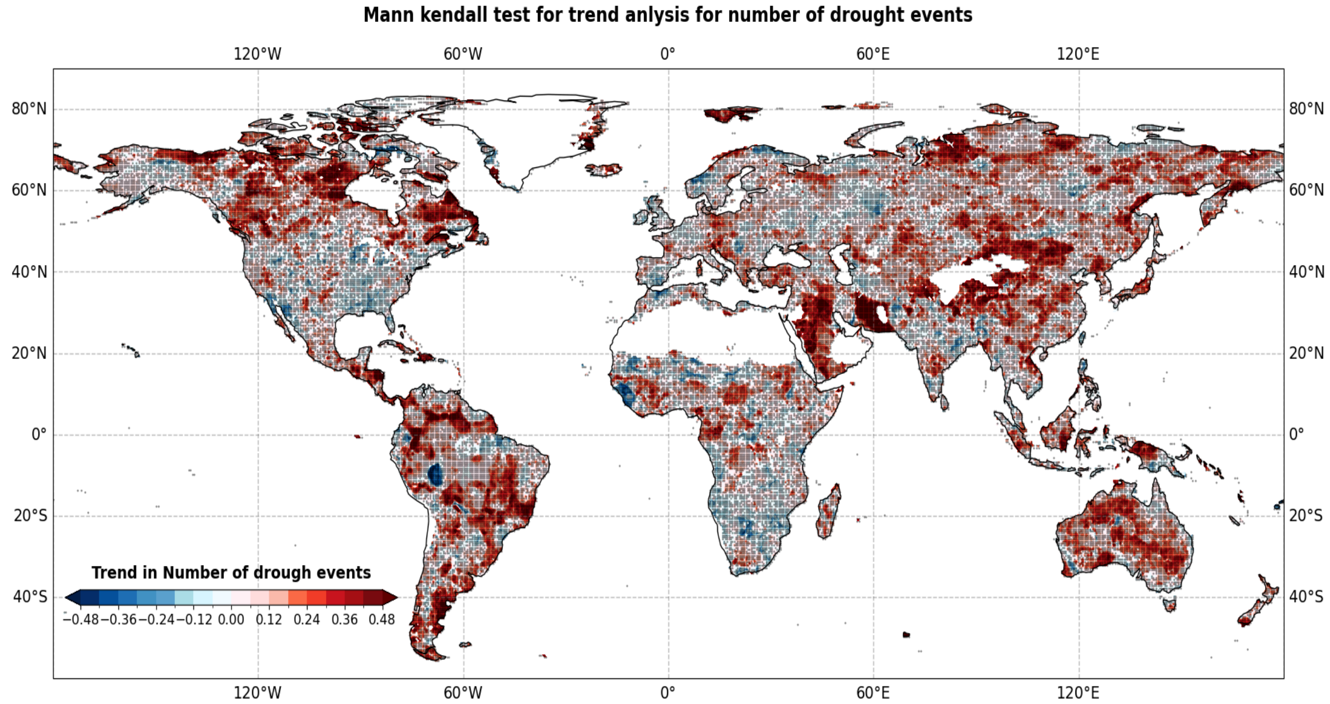

Supplementary Figure S4 Trends in the frequency of drought events in different periods using Mann Kendall test significant at $p<0.05$.

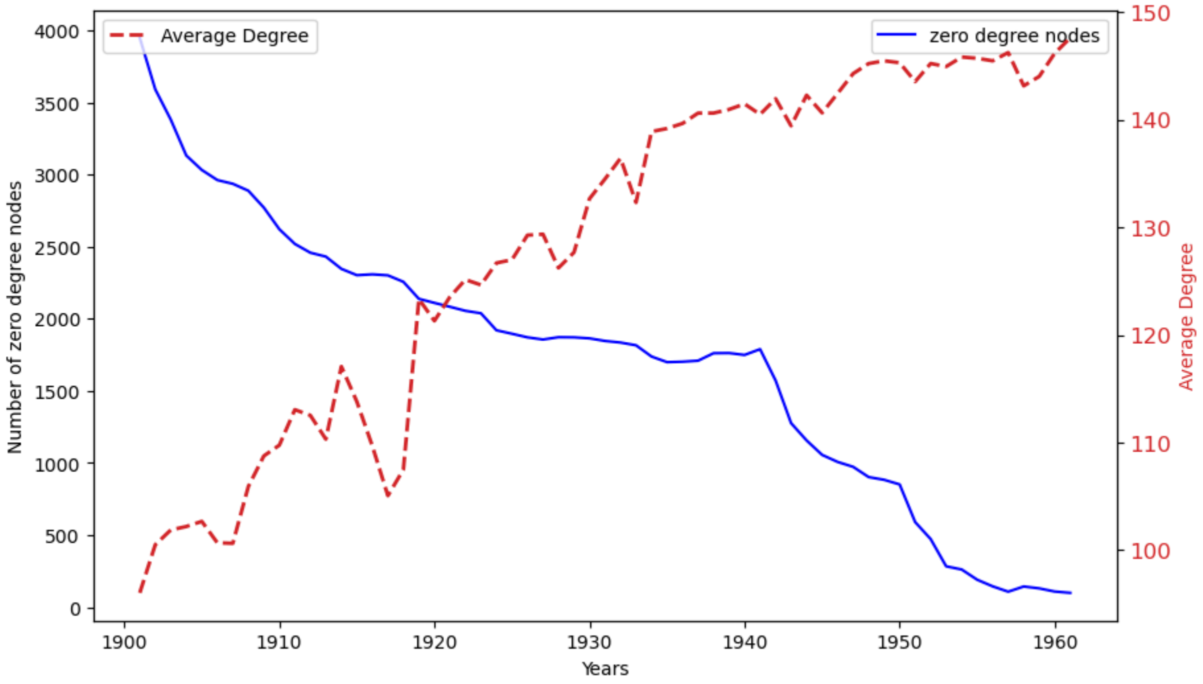

Supplementary Figure S5 Evolution of Number of zero degree nodes and average degree for the 61 instances of Complex network formed using sliding window approach.

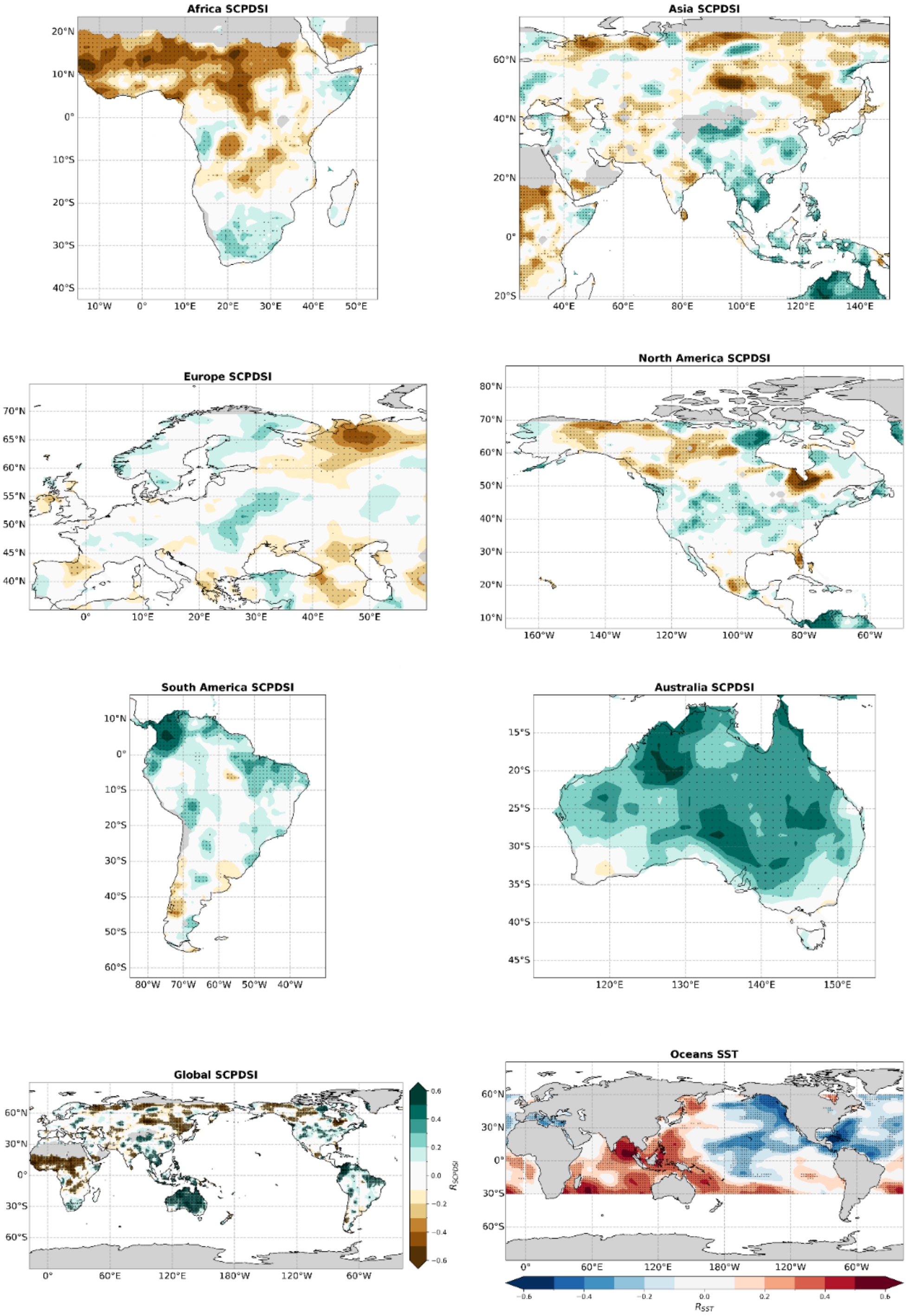

Supplementary Figure S6 Second modes of variability between scPDSI with sea surface temperature (SST) anomalies. The second mode of scPDSI-SST variability explains 15.17% of the squared covariance($r = 0.79, p < 0.05$).

(A) Second Mode (1901-1960) [SCF = 16.1 %, r = 0.89]

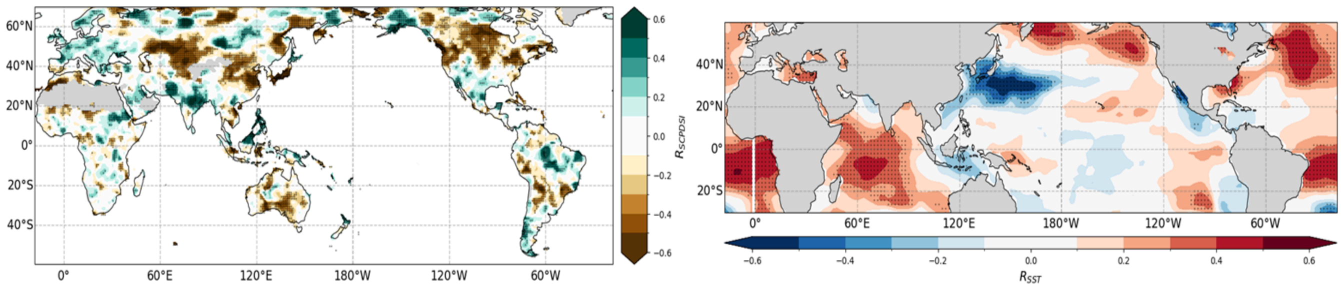

(B) Second Mode (1961-2020) [SCF = 17.6 %, r = 0.84]

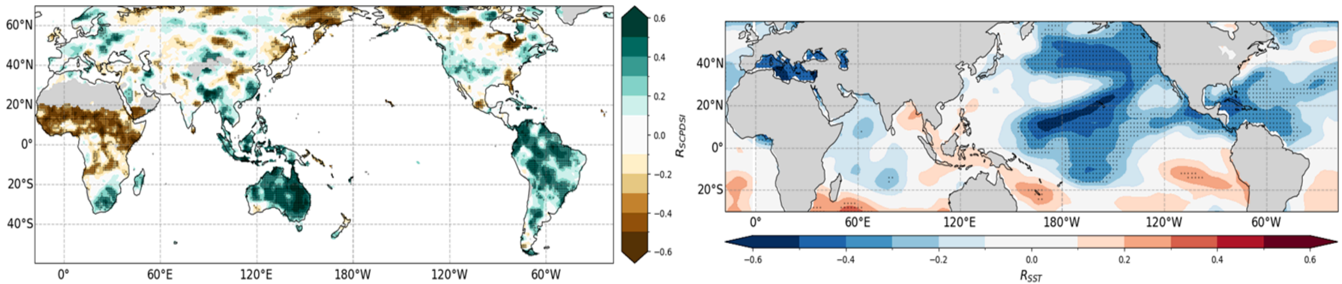

(C) Difference

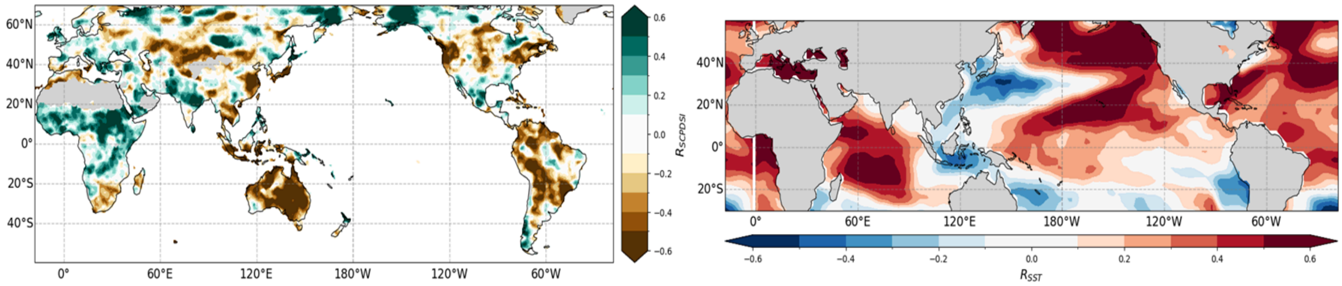

Supplementary Figure S7 Comparison of the MCA Analysis of sc-PDSI and SST Anomalies Between Two Periods (1901-1960 and 1961-2020)
(A) The Second mode obtained during the period of 1901-1960, the colored patterns are heterogeneous correlation coefficient between SST PC1 and sc-PDSI on land and sc-PDSI PC1 and SST departure field over ocean.**(B)**Same as **(A)** but for period of 1961-2020 **(C)** Difference between (1961 -2020) and (1901-1960)

(A)Second Mode P-SST (1901-2020)[SCF = 8.94%, r = 0.85]

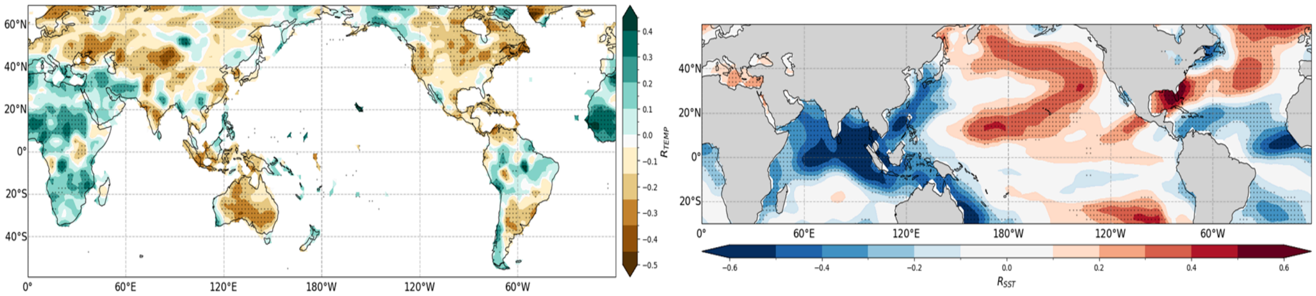

(B)Second Mode T-SST (1901-2020)[SCF = 18.8%, r = 0.67]

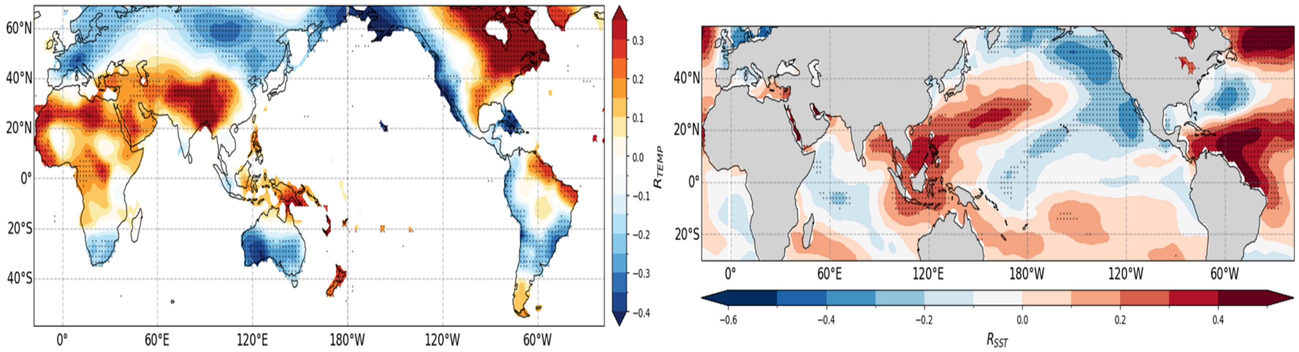

Supplementary Figure S8 Second modes of variability between precipitation (P) and temperature (T) with sea surface temperature (SST) anomalies. (A) The second mode of P-SST variability explains 8.94% of the squared covariance($r = 0.85$,$p < 0.05$). (B) The Second mode of T-SST explains around about 18.8% of squared covariance ($r = 0.67$,$p < 0.05$).The dominant influence of global warming has been removed from Global Temperature fields.

Supplementary Table 1 : Mean Conditional Probabilities of crop failure (Yield < $Y_{mean} - 0.5*Y_{std}$) given sc-PDSI <-2 across various continents based on the 1981-2016 global gridded crop data.

	Africa Above Equator	**Africa Below Equator**	**Asia**	**Europe**	**North America**	**South America**	**Australia**
Rice	**0.2824**	**0.3472**	**0.3367**	**0.3349**	**0.3602**	**0.3313**	**0.2559**
Maize	**0.2930**	**0.3335**	**0.3376**	**0.3861**	**0.4335**	**0.4018**	**0.2520**
Soybean	**0.2708**	**0.3444**	**0.3540**	**0.3995**	**0.5182**	**0.4198**	**nan**
Wheat	**0.2704**	**0.2677**	**0.3413**	**0.4031**	**0.4015**	**0.3747**	**0.3686**

Supplementary Table 2 Past ENSO Years based on Extended Multivariate ENSO Index (**ENSO YEARS LIST**)

El Niño	1900,1903,1906,1915,1919,1926,1931,1941,1942,1958, 1966,1973,1978,1980,1983,1987,1988,1992,1995,1998 2003,2007,2010,2016
Neutral	1901-1902,1905,1907-1908,1912-1914,1916,1920-1924 1927-1930,1932-1933,1935-1938,1940,1944-1949,1952-1954, 1957,1959-1961,1963-1965,1967-1970,1972,1975,1977,1979, 1981-1982, 1984-1986,1990-1991,1993-1994,1996-1997, 2001-2002,2004-2006,2009,2013-2015,2017-2020
La Niña	1904,1909,1910,1911,1917,1918,1925,1934,1939,1943,1950, 1951,1955,1956,1962,1971,1974,1976,1989,1999,2000,2008, 2011,2012

Supplementary Table 3 : Degree Centrality Statistics

Period	Mean DC	Std	Skewness	Kurtosis	Pr(Deg>X)
1901-1960	96	106	2.43	8.45	0.0347
1931-1990	134.5	111	6.55	143.7	0.0352
1961-2020	147	115	5.34	90.79	0.0474
1901-2020	182	152	3.09	19.15	0.099

X = 90th quantile of Degree Centrality from period 1901-2020

X = 357

Supplementary Table 4 : Trends in Degree and Average Link Length(ALL)

Continent	**Increasing ALL(%)**	**Decreasing ALL(%)**	**Increasing Degree(%)**	**Decreasing Degree(%)**
Africa	**57.54**	**41.83**	**71.43**	**28.22**
Asia	**30.91**	**67.15**	**66.41**	**32.49**
Australia	**58.91**	**31.25**	**88.51**	**11.49**
North America	**41.55**	**47.93**	**70.61**	**26.19**
South America	**35.53**	**51.66**	**52.48**	**34.85**
Europe	**41.56**	**50.10**	**75.47**	**23.83**